6. DIVERTOR

P. I. H. Cooke, C. G. Bathke, R. W. Conn, A. E. Dabiri,
W. P. Duggan, O. Fischer, S. P. Grotz, M. Z. Hasan,
R. A. Krakowski, F. Najmabadi, A. K. Prinja,
S. Sharafat, E. L. Vold, and K. A. Werley

CONTENTS

6. DIVERTOR

6.1. INTRODUCTION

An efficient mechanism for particle exhaust and impurity control will be an essential component of any magnetic fusion reactor, in order that the products of the fusion reaction can be removed and to avoid excessive contamination of the plasma core. In tokamak reactor studies much attention has been paid to this aspect of the design, both pumped limiters and magnetic divertors having been considered [1-3] but little work has been performed on impurity control systems for reversed field pinch (RFP) reactors. For the compact reversed field pinch reactor (CRFPR) [4,5], which represents the only major contribution to the field, a pumped limiter was used for the reference design although options for a divertor were also examined [5-7].

The limiter suffers from several drawbacks, particularly for a high power density device such as TITAN. Erosion is a potentially serious problem and because of the proximity to the plasma core this can represent a large source of impurities. Furthermore, to maintain the heat flux at an acceptable level in CRFPR [4], a core plasma radiation fraction, f_{RAD}, of 0.9 was used and 24 poloidal ring limiters covered 40 % of the first wall area. In a divertor design the region of high heat flux and plasma-surface interaction is removed to a separate chamber in a somewhat lower neutron flux and the probability of contamination of the core plasma by sputtered impurities is reduced. However, while divertors have been extensively employed with considerable success in present tokamak experiments, no RFPs have operated with a divertor, although divertor experiments are proposed in the ZT-H device at Los Alamos [8]. Nevertheless, a divertor has been selected as the primary approach for impurity control for TITAN.

In choosing the type of divertor to be used, a strong preference exists for selecting a configuration in which the minority magnetic field is nulled [6,7]. This choice minimizes the perturbations to the core plasma and reduces the engineering requirements in terms of coil currents, stresses, and power and energy requirements. For a RFP the toroidal field is weaker than the poloidal field and bundle divertors or toroidal-field divertors are the main options, whereas a poloidal-field divertor is more appropriate for a tokamak.

In the CRFPR study [5] the field line connection length was found to be too long for the bundle divertor, resulting in excessive cross-field diffusion to the first wall. On the other hand, the poloidally-symmetric toroidal-field divertor was considered a feasible design approach worthy of more detailed investigation. As the reactor parameters for TITAN are similar to those of CRFPR this recommendation has been followed and the symmetric toroidal divertor has been selected as the focus of the effort on impurity control for TITAN.

For the scoping phase of the project the work has concentrated on issues influencing the feasibility of the toroidal divertor concept. The magnet configuration is discussed in the next section followed by work on the modeling of the edge-plasma, including estimates of the conditions at the divertor target (see Sec. 6.3). The relationship between the first wall and divertor heat loads is described in Sec. 6.4 and the various heat removal concepts that have been considered are discussed in Sec. 6.5. Finally, conclusions from the work performed so far are presented, followed by plans for further work during the next phase of the project.

6.2. DIVERTOR MAGNETICS

6.2.1. Basic Configuration

For this phase of the project the coil layout has been determined using a two-dimensional analysis of the magnetics, including only the toroidal field (TF) coils and the divertor coils. A full three-dimensional simulation, including the effects of the plasma and the poloidal field (PF) coils, will be carried out in the future and the importance of this analysis is described in Sec. 6.2.3.

A plan view of a typical coil layout is shown in Figure 6.2.-1 and a magnified view of the outboard side is given in Fig. 6.2.-2. The figures show the divertor coils and the TF coils and field lines near the inboard and outboard edges of the plasma; in reality, the rotational transform provided by the plasma current and the PF coils would link these two sets of field lines. The divertor coils comprise the central nulling coil, whose current opposes that of the TF coils, and two flanking coils, which have currents in the same direction as the TF coils. The sum of the divertor coil currents is always zero to minimize the effect of the divertor on the global magnetic configuration.

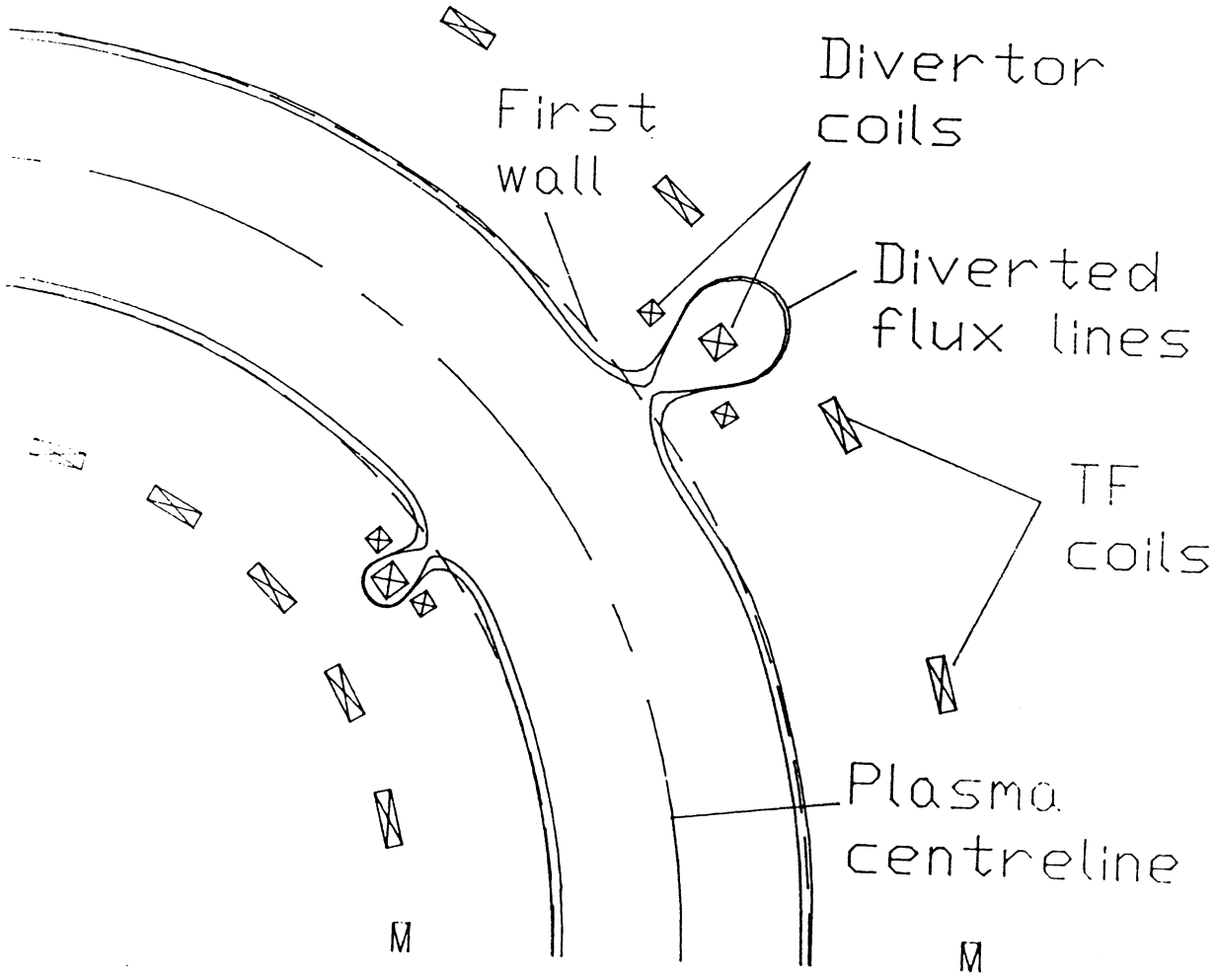

Fig. 6.2.-1. A plan view of a typical coil layout for a symmetric toroidal - field divertor showing the TF coils, divertor coils and diverted field lines on the inboard and outboard sides (generated with a 2-D magnetics analysis).

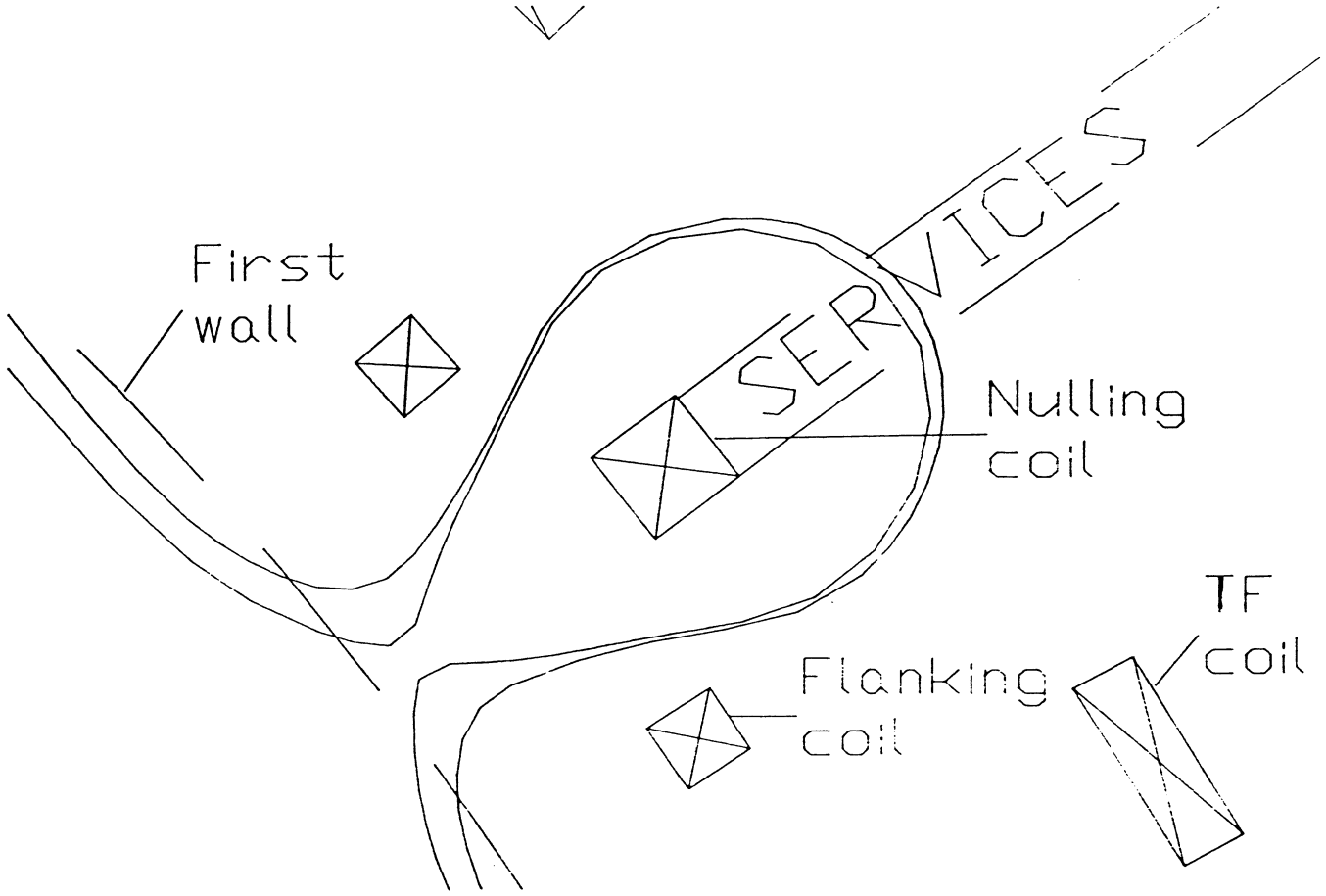

Fig. 6.2.-2. A magnified view of the outboard side of Fig. 6.2.-1, also showing a notional access corridor (labeled "services").

In Fig. 6.2.-2 an access corridor is shown (labeled "services") behind the nulling coil to illustrate the region through which coolant and support structure must pass. This access is only provided at one poloidal location or over a limited range of poloidal angle. A poloidally continuous and cooled divertor target is located on each side of the service corridor to neutralize the incident plasma.

Several sets of divertor coils may be located around the torus. To minimize the heat flux at the divertor plate and to reduce the field line connection length a large number of divertors is desirable. The penalties for including more divertors are a larger Ohmic power loss in the divertor coils and a removal of potential breeding blanket volume which has a detrimental effect on the global tritium breeding ratio. Following references [5,7], the number of divertors has been set at 4 for the preliminary analysis for TITAN.

The divertor coils are located so as to produce the required degree of diversion of the field lines, i.e. to locate the separatrix at the plasma surface. This requirement forces the coil centers to be offset from the plasma centerline to ensure an equal diversion of inboard and outboard field lines at the same minor radius. In determining the coil radius, sufficient space must be allowed behind the first wall to provide a minimum shield for the coil from the high neutron flux. An examination of life-limiting processes for highly irradiated normal-conducting magnets is now in progress, and a shield thickness of 10 cm is currently specified to restrict radiation damage in the coil insulator to allowable levels. The coil current densities are chosen to ensure that no field line intersects any coil.

The field line plot in Fig. 6.2.-2 shows that the divertor configuration is not of the "open" nature which is generally obtained in tokamak reactors with poloidal divertors. This difference arises from the positioning of the divertor coils. For a tokamak reactor the poloidal divertor configuration is usually produced by remote PF coils which are external to the TF coils, resulting in a wide spreading of the open field lines outside the separatrix (i.e., similar to the expanded boundary geometry obtained in Doublet III [9]). The toroidal divertor configuration of the RFP reactor is generated with coils which are placed close to the plasma surface and the open field lines remain more tightly bound. This "closed" divertor configuration is beneficial as it allows the divertor chamber to be decoupled from the main plasma chamber, whereas in a tokamak with an open poloidal divertor the divertor chamber is merely an extension of the main plasma chamber. Baffles or constrictions in the wall of

the closed divertor geometry enable neutral gas backflow to be minimized and the neutron damage at the divertor plate should be substantially lower than at the first wall. A disadvantage of the closed geometry is that the spacing between the field lines tends to reduce in the divertor resulting in an increase in the heat flux on the divertor target as the plasma strikes a smaller area. The possibility of spreading these field lines is considered in Sec. 6.2.4.

6.2.2. Integrated-Blanket-Coil Divertor

6.2.2.1. Concept

The Integrated-Blanket-Coil (IBC) concept combines the blanket functions of tritium breeding and energy recovery with the coil function of magnetic field production in a single component. Specifically, electrical current is passed through a flowing liquid lithium blanket, which also serves a coil function. This concept is considered for use in conjunction with the liquid metal cooled blanket only. Several benefits can be anticipated from adopting the IBC approach for divertor coils:

1. Radiation damage to the conductor and insulator is not a concern. This minimizes the need for shielding and allows the coils to be placed closer to the plasma.

2. Magnetic coupling is improved when the coils are moved closer to the plasma, reducing current requirements.

3. The breeding and energy recovery medium is present in the volume normally displaced by the copper coils and shielding. This will improve the tritium breeding ratio and the thermal power output.

4. Ohmic losses incurred in the IBC are deposited at a temperature that allows recovery in the thermal cycle.

The major drawback to the IBC concept is the high electrical resistivity of liquid metals, such as lithium, which, at coolant temperatures, is about 13 times that of a wound copper coil operating at 300 K. Some of this difference is compensated, as noted above, by recovering the Joule losses in the IBC coil,

so that some 35-40 % of the Ohmic heat reappears as electrical power. Further reduction of the power loss can be accomplished through improved coupling of the divertor-plasma magnetics and lower current density in the IBC.

Preliminary analysis indicates that a combination of vanadium alloy structure and lithium is attractive for use with the IBC. Selection of these materials is consistent with the Blanket Comparison and Selection Study [10], which rated the Li-V option as the primary choice for the self-cooled liquid metal blanket. For this study, therefore, the IBC has been taken to consist of: (1) liquid lithium as the tritium-breeding material, electrical conductor, and heat transfer medium; and (2) a vanadium alloy such as V-3Ti-1Si as the structural material.

6.2.2.2. Results

An IBC divertor configuration was determined for comparison with an earlier divertor design using conventional coils [5,7]. Table 6.2.-I summarizes the parameters of the two configurations, while Figure 6.2.-3 shows the field lines for a typical coil layout for the IBC version. The case considered corresponds to a neutron wall loading of about 20 MW/m^2. Lower wall loadings lead to lower field strengths on edge, and thus reduce the nulling current and corresponding Ohmic losses.

6.2.2.3. IBC Coil Design

The IBC divertor coils would use a two-pass flow pattern where the lithium would enter the coil and make a poloidal loop, then reverse direction and make another poloidal loop before exiting to the heat exchanger. This allows both the inlet and outlet to be at the same electrical potential (ground), which eliminates leakage current paths. A penalty is incurred, however, in that the coolant must flow about twice as fast to cover the longer flow path with the same rise in temperature, resulting in relatively high MHD pressure drops.

A sandwich design is used to mitigate these MHD pressure losses, with electrical insulator separating the structural material from a very thin surface conducting layer. The voltage in the divertor nulling coil is about 60 V, indicating that a ceramic insulator such as MgO or spinel would provide adequate insulation even with a degradation of resistivity of 3-4 orders of magnitude due to the ionizing radiation flux. Use of such a sandwich design would keep the maximum MHD pressure drop in the divertor system to less than 3 MPa.

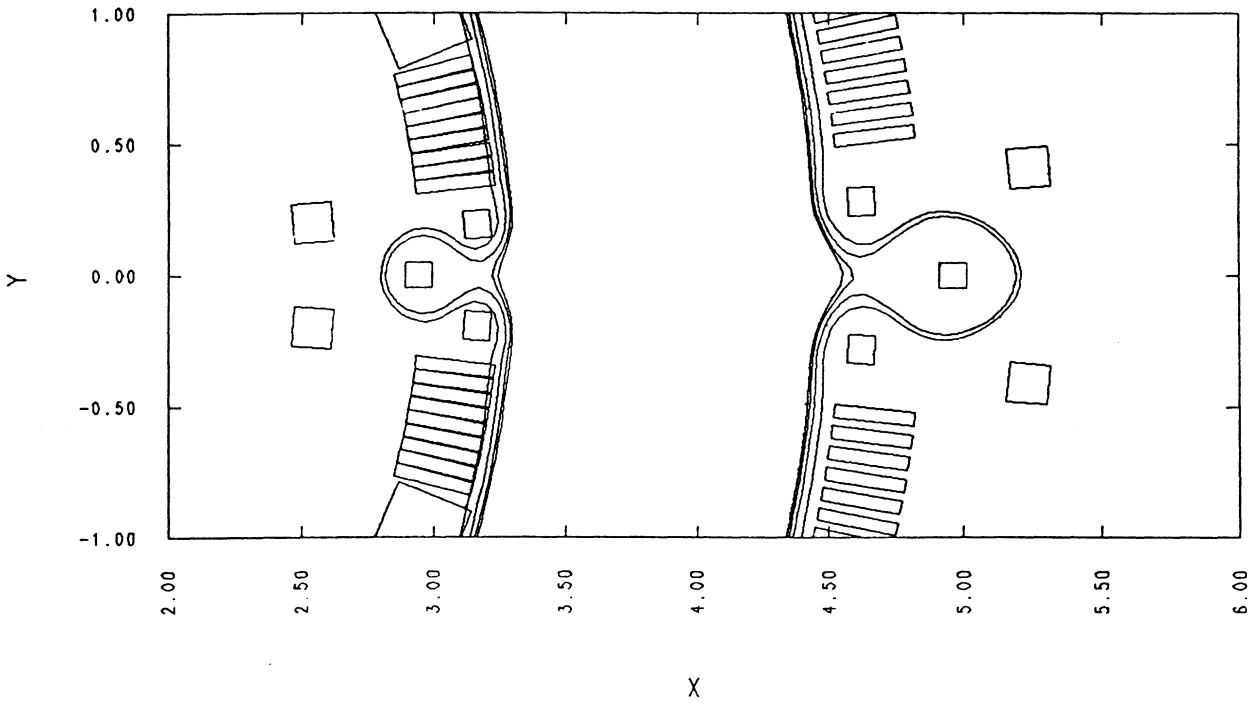

Fig. 6.2.-3. A typical 2-D field line plot for the IBC divertor design.

TABLE 6.2.-I
Divertor Coil Design Parameters

	Conventional	IBC
NULLING COIL		
Current (MA)	0.8	0.3
Current Density (MA/m^2)	50	28
Coil radius (m)	1.088	1.002
FLANKING COILS		
Current (MA)	0.4	0.15
Current Density (MA/m^2)	40	24
Coil radius (m)	0.97	0.87
OHMIC POWER (MW)	48.4	118.1

6.2.3. Three-Dimensional Modeling

The two-dimensional modeling of the TITAN divertor only simulates the toroidal and radial magnetic fields and yields two-dimensional field-line tracings of the kind shown in Fig. 6.2.-4 for the CRFPR design [5,7]; these computations are used to locate the separatrix. The global alignment of the separatrix with the plasma surface is used to determine the divertor-coil currents and geometry. The two-dimensional field-line tracings can also be used to estimate the connection length between successive divertor throat openings, with an accuracy of ~ 10% based on the CRFPR results [5,7], to yield a qualitative estimate of the effect of the divertor on the toroidal-field ripple, and to locate the flux plume within the divertor chamber.

The three-dimensional modeling simulates the toroidal, radial, and poloidal components of the magnetic field and yields three-dimensional field-line tracings which are represented as puncture plots in Figs. 6.2.-4 and 6.2.-5 for the CRFPR design [5,7]. Adding the poloidal dimension to the two-dimensional (radial and toroidal) simulation permits the expression of the purely three-dimensional phenomena of magnetic islands and flux surface broadening. The magnetic islands are the result of the beating of the resonant helical pitch of a field line with the toroidal field ripple, whereas flux surface broadening occurs because of poloidal asymmetries in the toroidal field ripple. If the

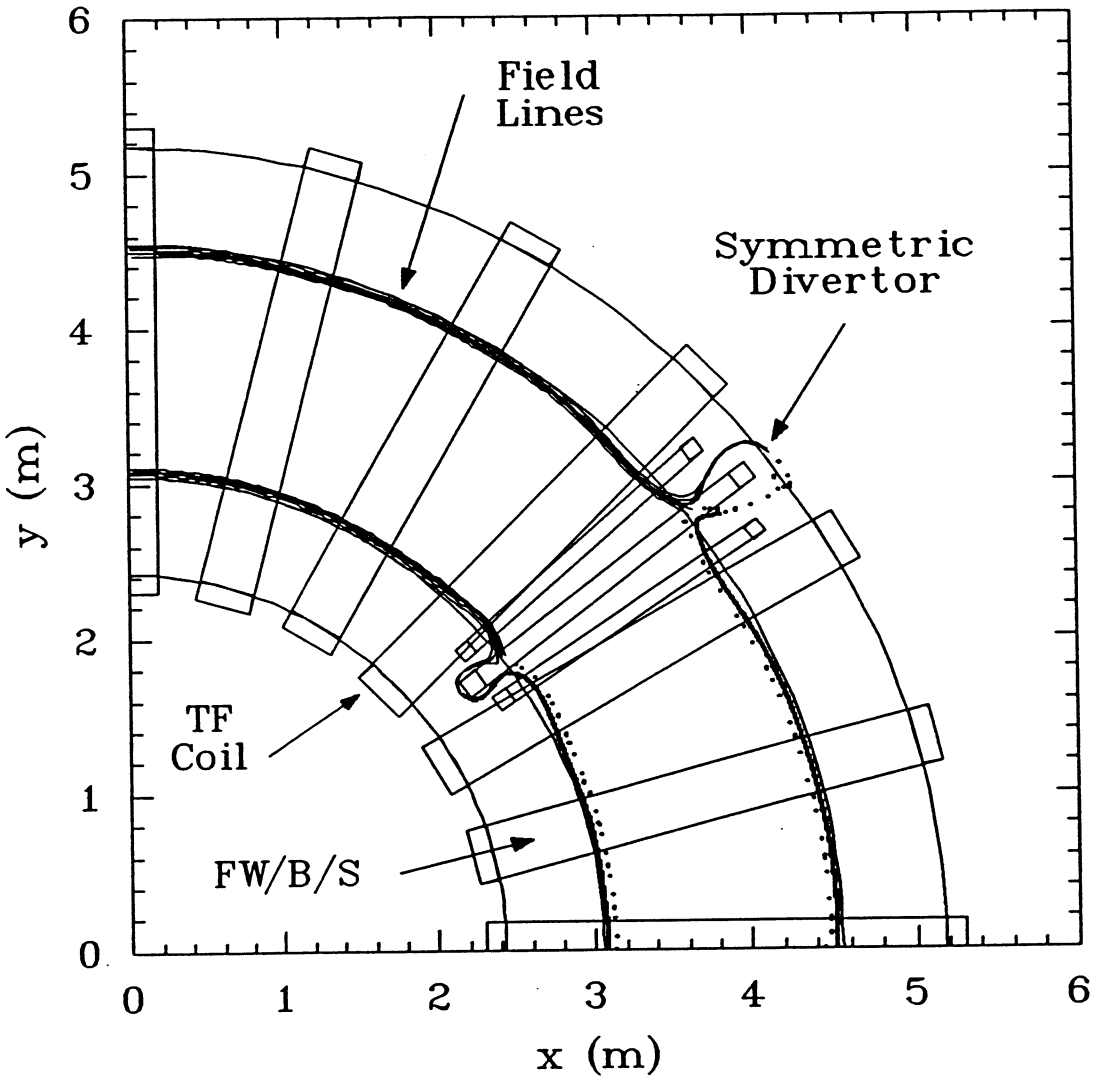

Fig. 6.2.-4. The equatorial-plane view of the two-dimensional field-line tracings (solid lines above and to the left of divertor) for the four symmetric divertors of the CRFPR design [5] at minor radii of r = 0.69, 0.705, 0.715, 0.73, and 0.75 m. The plasma minor radius is 0.71 m. Also shown (below and to the right of divertor) are the puncture plots (the field-line intersections with the equatorial plane) for the three-dimensional simulation of plasma and all coils at minor radii of r = 0.68 and 0.73 m. The toroidal-field (TF) and divertor coils are also shown. This figure is taken from reference [7].

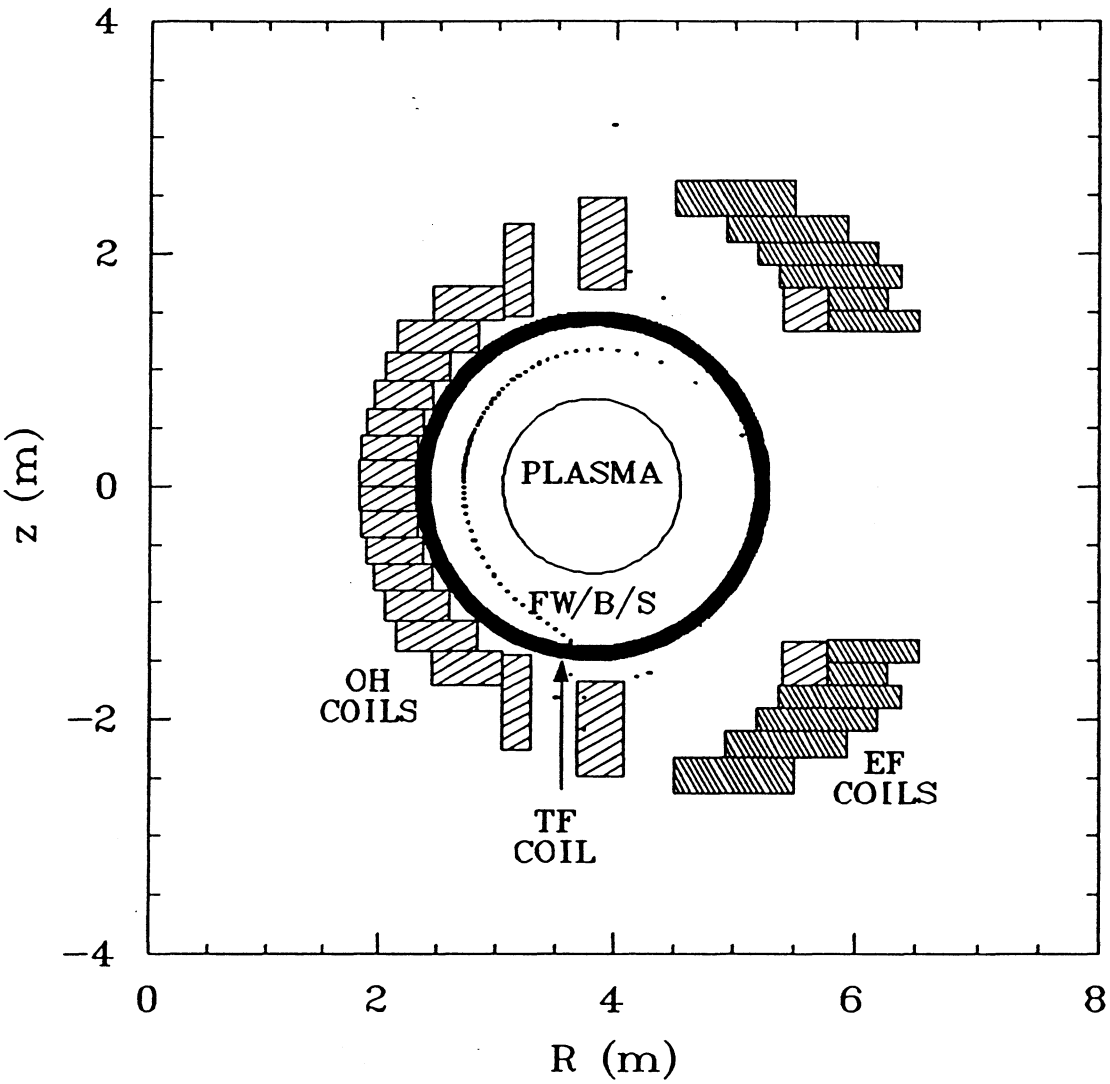

Fig. 6.2.-5. The cross-sectional view of the puncture plots (the field-line intersections with the divertor-coil plane) for the three-dimensional simulation of plasma and all coils. The Ohmic-heating (OH), equilibrium-field (EF) and toroidal-field (TF) coils are also shown, based on the coil set for CRFPR.

flux surfaces between the plasma surface and the reversal surface become sufficiently broadened to overlap the latter two surfaces, then both energy and particle confinement will be lost in this region, which is considered to be responsible for most of the confinement in the RFP. Consequently, tracing at least one field line between the reversal and separatrix surfaces is necessary to ensure that the divertor has not introduced a toroidal-field ripple that is too large.

The inboard-to-outboard asymmetry displayed in the two-dimensional field-line tracings of the divertor plume, which is the result of the toroidal field being inversely proportional to the major radius, produces effects that can only be seen with three-dimensional field-line tracings outside the separatrix. The stronger inboard toroidal field, relative to the outboard toroidal field, results in field lines bunching together poloidally, with a factor of more than four compression over a uniform distribution for the case shown in Fig. 6.2.-5. The precise location of the poloidal peak in field-line density is a function of edge-plasma q-value, plasma major radius, and average radial extent of the divertor plume; a three-dimensional field-line tracing within the scrape-off layer is needed to locate this maximum field-line density. If a collector plate is to be positioned within the divertor chamber to minimize this peaking, then three-dimensional field-line tracing in the scrape-off layer is the only method which yields the necessary geometrical information for positioning the collector plate. In addition, the poloidal variation in the toroidal field and the radial variation in the poloidal and toroidal fields make three-dimensional field-line tracings the only method for accurately determining the connection length between successive divertor collector plates with an accurate determination of the connection length between successive divertor-throat openings as a valuable by-product.

The divertor design for TITAN has not yet proceeded sufficiently to yield three-dimensional results. When a divertor configuration has been determined from the two-dimensional simulations, the configuration will be subjected to three-dimensional analysis and iterated upon until an acceptable design is obtained.

6.2.4. Flux Expansion in the Divertor Chamber

It was observed earlier that the "closed" nature of the divertor configuration for TITAN gives rise to a compression of the field lines in the divertor chamber. In order to reduce this effect, which tends to increase the

heat loading on the divertor target, the possibility of including extra divertor coils to modify the flux surfaces was briefly investigated.

Figure 6.2.-6 gives a view of the outboard field lines for a case with one extra nulling coil located in the same plane as the primary nulling coil but at a larger radius. The flux surfaces have clearly been altered and the spacing between the field lines has increased somewhat in the vicinity of the additional coil. However, the effect is only modest and only occurs over a relatively small region. Other cases with the addition of further coils were examined but no large scale expansion of the flux surfaces was found. The difficulty arises from the need to generate a large region of space in which the magnetic field is decreased (which tends to increase the separation between field lines) which is not possible with only a small number of coils located close to the main divertor coils. As the inclusion of the extra coils adds significantly to the complexity of the divertor design and the benefits are relatively small it was concluded that such a modification is not worthwhile.

6.3. EDGE-PLASMA MODELING

The main aims of edge-plasma modeling for a fusion reactor are to predict the plasma conditions at the first wall and divertor target and to estimate the requirements for particle removal. The heat flux distribution and erosion rate from sputtering are important considerations for the divertor design and the pumping speed required from the vacuum system governs the size of the vacuum ducts.

For the scoping phase of the TITAN project work has concentrated on estimating the peak heat flux on the divertor target and on ways to reduce the load to a manageable level. Both analytic and computational models have been used and more detailed analysis is planned for the next phase of the project.

6.3.1. Estimates of Scrape-off Layer Parameters

6.3.1.1. Analytic Model

A simple model developed by Harbour for a tokamak poloidal divertor [11] has been used to estimate the characteristic thickness for the radial decay of power flow in the scrape-off layer and the plasma temperature at the divertor target. The geometry of the model has been modified to make it applicable to an RFP reactor with several toroidal divertors. In this model the scrape-off layer

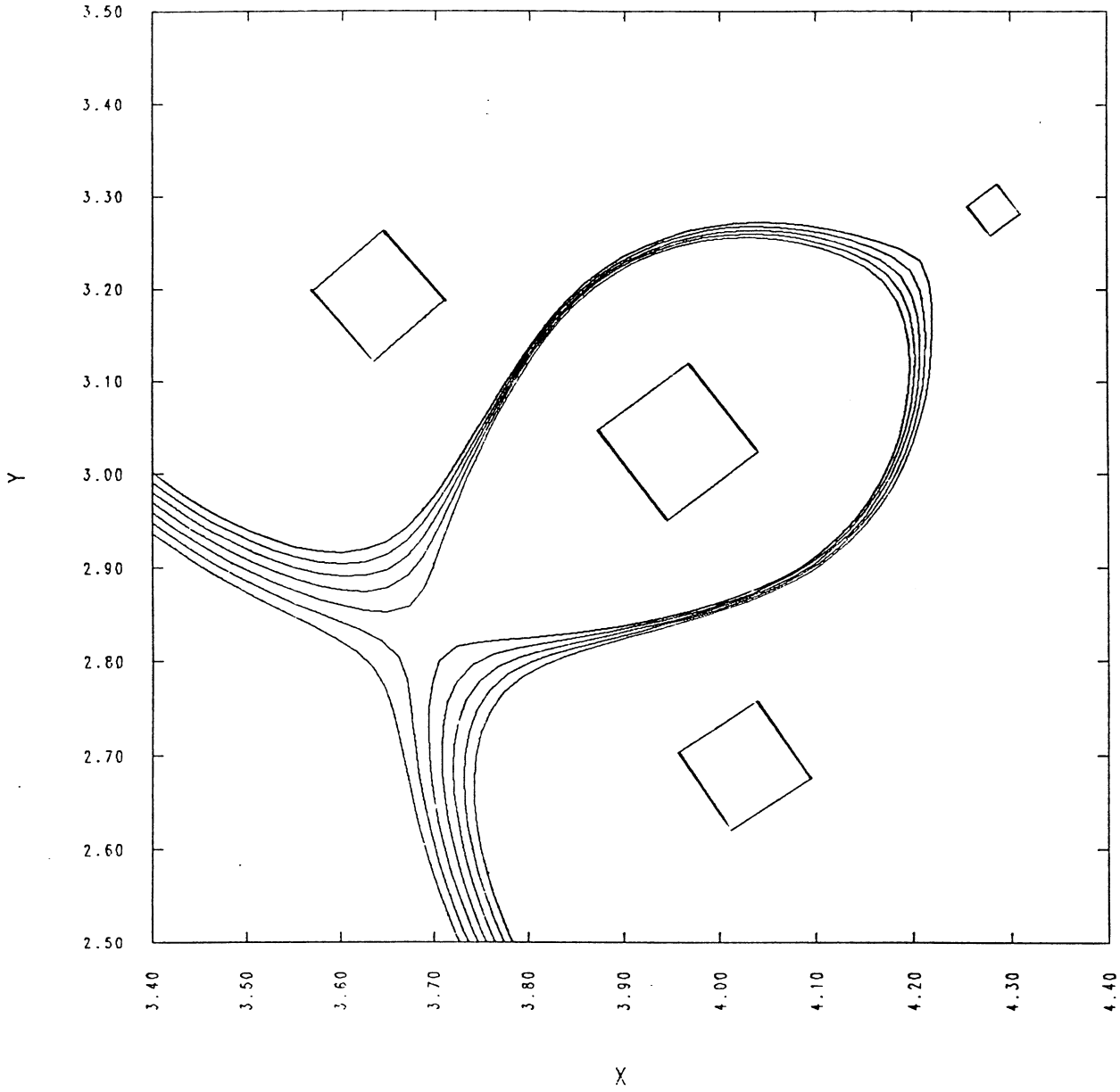

Fig. 6.2.-6. A view of the outboard field lines for a case with an extra nulling coil behind the primary nulling coil to investigate the possibility of flux expansion in the divertor.

is treated as a slab of thickness λ_{SOL} with no radial variation of parameters across the slab. The thickness evaluated in the model may be interpreted as a radial e-folding length or gradient scale length for power flow. Power flow parallel to the magnetic field is assumed to occur by electron conduction alone except for the convective energy transfer through the sheath at the target.

Input parameters for the model include the geometry of the scrape-off layer (major radius, minor radius, field line connection length etc.), the total power, P_D, crossing the separatrix, the number of divertors, N_D, and the radial thermal diffusivity, $\chi_\perp$. The plasma temperature at the divertor target, T_t, and at the midpoint between two divertor entrances, T_s, the density at the target, n_s, and the gradient scale length for power flow, λ_{SOL}, are then determined as a function of the density at the midpoint between two divertors, n_s.

Fig 6.3.-1 shows a set of results for the 20 MW/m^2 TITAN design, for the case when P_D = 250 MW (f_{RAD} = 0.5). For upstream plasma densities, n_s, of ~ 1 - 2 x 10^{20} m^{-3}, λ_{SOL} is ~ 1 cm and the plasma temperature at the target, T_t, exceeds 100 eV. Such a short scale length will lead to very high heat fluxes on the target, while the high temperature will result in severe sputtering of the target. The reason for the small thickness of the scrape-off layer for power flow lies in the dominance of parallel over radial heat transport. The high conductivity associated with parallel electron heat conduction ($\propto T^{5/2}$) causes heat to be lost axially at a rapid rate compared with the radial loss, even for the relatively high value of radial thermal diffusivity, $\chi_\perp$, of 4 m^2/s, which is assumed here.

At higher values of n_s the situation improves with λ_{SOL} increasing and T_t falling. However, an upper limit exists for n_s, as it clearly cannot exceed the average core plasma density, $\bar{n}$, indicated on the figure, and is likely to be lower by a factor ~ 2 - 4. If the total power, P_D, being transported to the divertor is reduced (i.e. higher f_{RAD}) then λ_{SOL} also increases and T_t decreases, but this change would also imply a higher heat flux on the first wall.

Thus, this simple analytic model suggests that the scrape-off layer thickness for power flow is unlikely to be much greater than 1 cm and that the plasma temperature at the target will be high, unless the total power flowing to the divertors can be reduced.

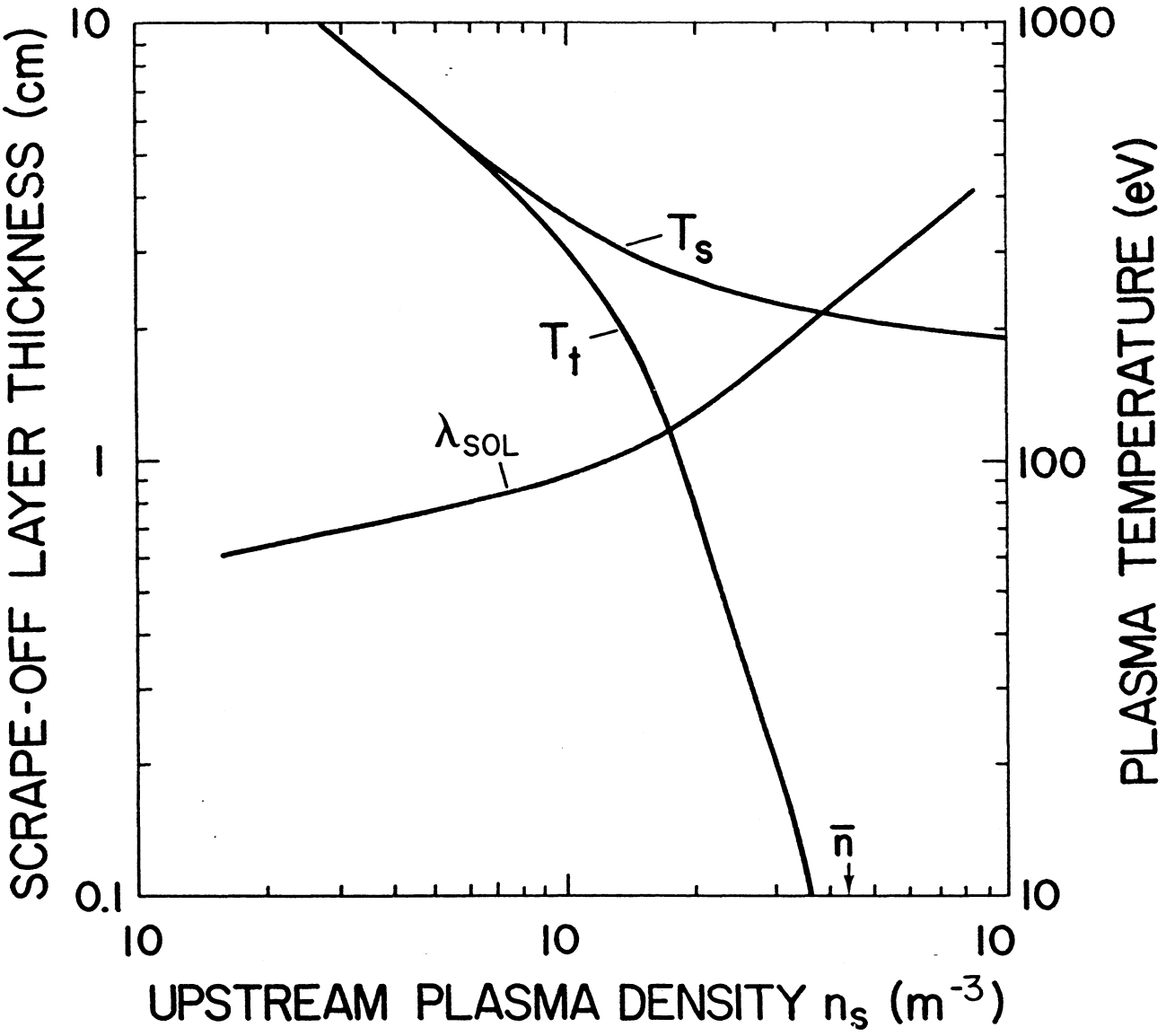

Fig. 6.3.-1. Results from an analytic model [11] of the TITAN scrape-off layer, showing the variation of the scrape-off layer thickness and the upstream and target plasma temperatures as a function of the upstream density.

6.3.1.2. Computational Model

Analytic models of the scrape-off layer are very valuable in identifying basic scalings and trends of the key plasma parameters but the broad assumptions which have to be made in such models render any quantitative conclusions somewhat uncertain. Numerical models, however, allow many more physical processes to be considered and are necessary for more accurate calculations at a well defined design point.

An axially averaged radial transport model of the scrape-off layer called ODESSA (One-Dimensional Extended Scrape-off Simulation and Analysis), is being used to model the TITAN edge plasma. A description of this code is given in references [12] and [13]. The two-dimensional scrape-off layer is divided axially into two regions, as shown in Fig. 6.3.-2, representing the upstream and downstream regions. The first region represents the edge-plasma adjacent to the main plasma and is fed with particles and energy from the core. In this region radial transport is dominant and parallel gradients are weak. The downstream region is dominated by recycling neutrals near the divertor target and radial transport is neglected in comparison with the rapid parallel transport due to the near sonic plasma flow in this region.

Output from the model is in the form of radial profiles of density, ion and electron temperature, and particle and energy fluxes for each region. Figs. 6.3.-3 and 6.3.-4 show density and temperature profiles respectively from a preliminary run for the TITAN scrape-off layer. The scrape-off layer width was taken as 5 cm as assumed for the systems code (Sec. 5) and the upstream separatrix density was taken as approximately 2×10^{20} m^{-3}. The power transported to the scrape-off layer was in accordance with a core radiation fraction, f_{RAD}, of 0.5 and the recycling coefficient at the target was uniform across the radius at 0.99. There are several unsatisfactory features on these curves indicating the need for further work to adjust the plasma parameters to acceptable levels.

Firstly the upstream plasma temperature at the wall is high, ~ 80 eV, which combined with the steep density gradient at the first wall, will lead to an unacceptably high sputtering rate of the wall. The peak downstream (or target) plasma temperature is also too high, at over 100 eV. Sputtering due to high energy ions accelerated through the sheath potential would be excessive. Both of these problems will be alleviated with the inclusion of impurity radiation and improved models of neutral recycling at the wall and target which will be incorporated into the code during the next phase of the project (Sec. 6.3.4).

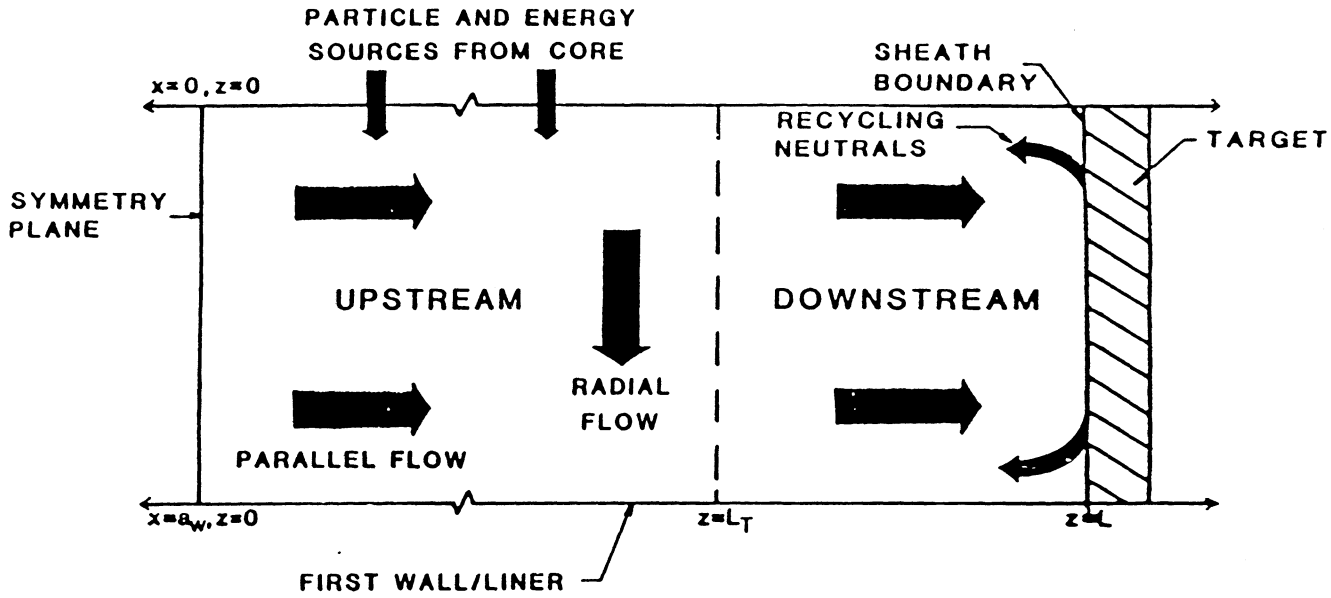

Fig. 6.3.-2. Schematic of the edge-plasma showing the division into upstream and downstream zones as used in the ODESSA plasma transport code.

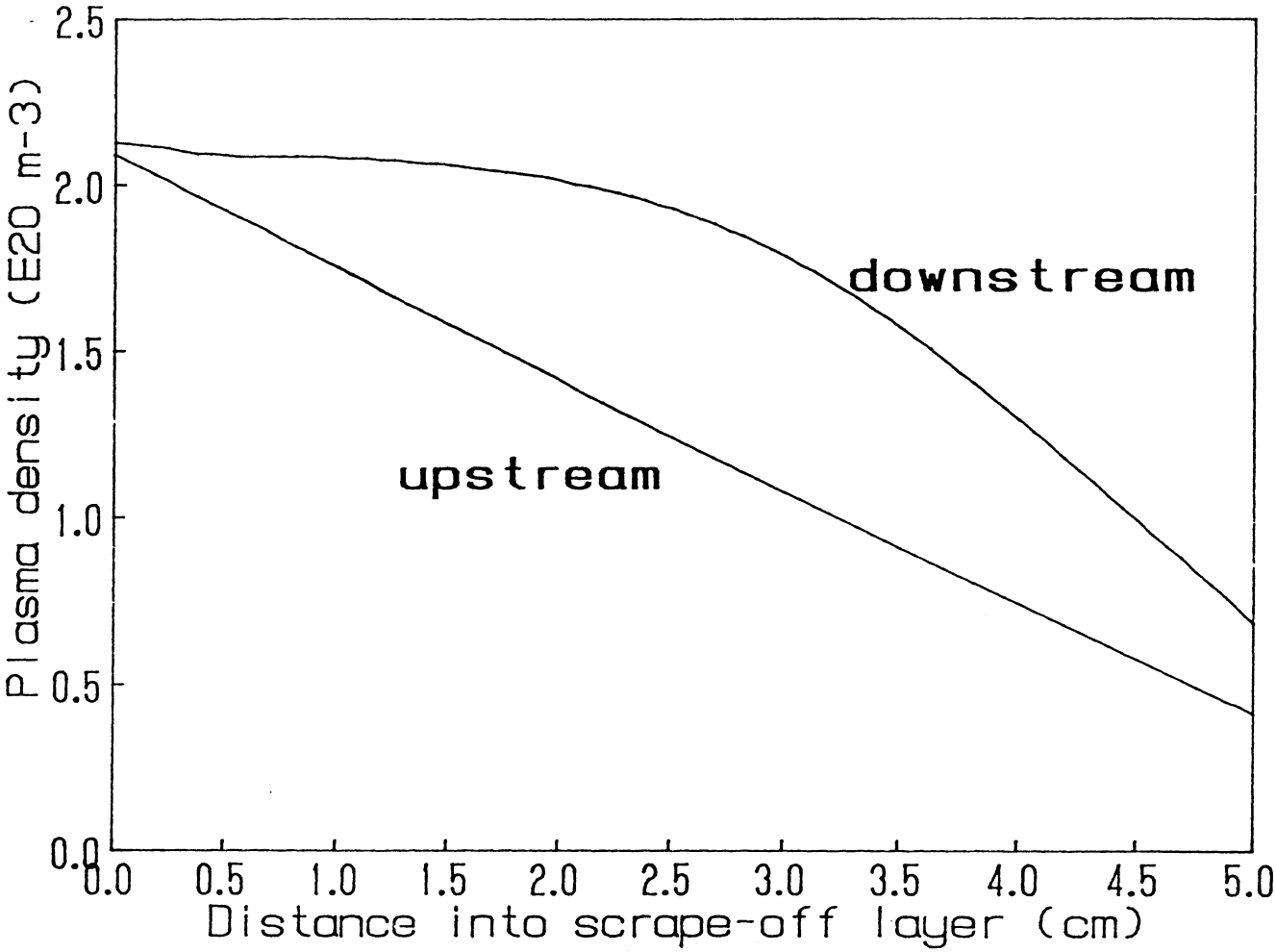

Fig. 6.3.-3. Upstream and downstream radial profile of plasma density for f_{RAD} = 0.5 (P_D = 250 MW).

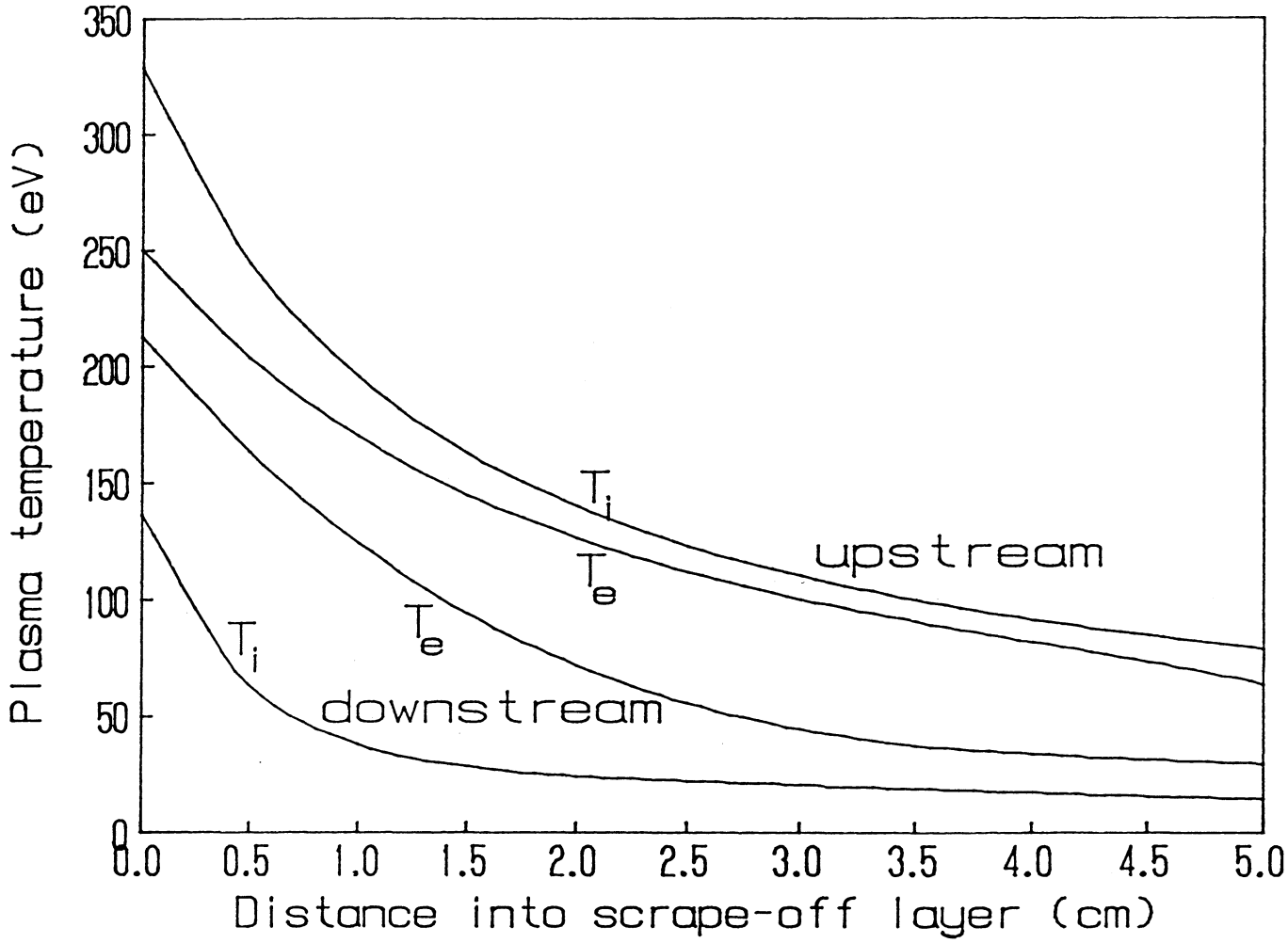

Fig. 6.3.-4. Upstream and downstream radial profiles of electron and ion temperature for f_{RAD} = 0.5 (P_D = 250 MW).

The heat flux into the sheath falls off approximately exponentially with radius with an e-folding length of close to 1 cm, in good agreement with the prediction of the analytic model.

6.3.2. Peak Heat Loading on the Divertor Target

The gradient scale length for power flow in the scrape-off layer, as determined in Sec. 6.3.1, can be used to estimate the peak heat flux on the divertor target. One point which should be borne in mind, however, is that the characteristic thickness of the scrape-off layer for power flow evaluated by plasma models applies in the region adjacent to the core plasma and, because of radial diffusion and changes in magnetic field strength, may be different at the divertor target. The flux plots in Section 6.2 show that the plasma will be slightly compressed in the divertor chamber (by a factor of ~ 2); but this tendency to increase the heat loading will be offset by radial diffusion within the divertor, especially in the vicinity of the sharp peak in the approximately exponential power profile as it enters the source-free region downstream of the null point. As an approximation in estimating the peak heat load on the target these two effects are assumed to cancel and an unchanged radial power profile is used.

For a target placed in the shadow of the nulling coil perpendicular to the flux surfaces (in the region labeled "services" on Fig. 6.2.-2), the peak heat load, q_{PK}, is given by

$$q_{PK} = \frac{P_D}{2N_D\ 2\pi a_D \lambda} \qquad (6.3.-1)$$

where P_D (= $[1 - f_{RAD}][P_\alpha + P_\Omega]$) is the total power removed by the divertors, N_D is the number of divertors (the factor 2 allows for two targets per divertor), a_D is the average minor radius of the divertor target and λ is the e-folding length for the power flux at the divertor target.

Taking P_D = 250 MW (f_{RAD} = 0.5), N_D = 4, a_D = 1.2 m and λ = 1 cm this yields a peak power load of ~ 400 MW/m^2, ignoring any peaking factor due to the poloidal asymmetries described in Sec. 6.2.3. Such a heat flux is well beyond the limit for any steady-state heat removal system, but there are many ways to reduce the loading. The major factors which influence the peak divertor power load are indicated below:

- Radial scale length for power flow
- Core plasma radiation fraction
- Divertor plasma radiation
- Number of divertors
- Divertor connection length
- Divertor target inclination
- Flux expansion in divertor
- Diffusion in divertor
- Ergodic field lines
- Plume oscillation

The radial scale length for power flow is the key parameter in determining the divertor heat flux. Its magnitude depends on the relative rates of parallel and radial heat transport, as explained in Sec. 6.3.1, and the value of $\lambda = 1$ cm used for the estimates of heat load seems appropriate for the TITAN divertor conditions.

An increase in the core radiation fraction will reduce the power flowing to the divertors but it will increase the load on the first wall; the relationship between the first wall and the divertor heat loads is described in Sec. 6.4.

Radiation from the divertor plasma will spread the heat load over the divertor chamber walls, but the line-radiation from the DT exhaust plasma will be small at the high densities expected in the divertor. Impurities with high atomic number, Z, injected into the divertor plasma, however, will radiate strongly and might result in a large reduction of the target heat loading. This possibility is examined further in Sec. 6.3.3.

The number of divertors could be increased but this change would also remove breeding blanket space and increase the resistive losses in the divertor coils. The choice of $N_D = 4$ represents a first estimate of an overall optimum configuration.

Perhaps the most direct approach to reduce the heat load is to incline the target at an angle to the incident plasma stream. Uncertainties in the plasma position and, hence, in the location of the exhaust plume, impose a limit on how obliquely the target may be inclined and an angle of 8° was specified in reference [14]. In this case the loading is reduced by a factor of $(\sin 8°)^{-1} \simeq 7$.

The possibility of expanding the flux in the closed divertor configuration with the use of extra coils was considered in Sec. 6.2.4 and it was concluded that any benefit to be obtained was slight and localized. Radial diffusion in the divertor plasma will tend to increase the thickness of the plasma channel but this effect was included in the heat load estimated above.

The last two effects are expected to have a small effect on the divertor heat load. The ergodicity of the field lines in the divertor, discussed in reference [5], will smear the power over a slightly greater area than predicted above. Oscillation of the plasma due to the F-Θ current drive (Sec. 4.6) may cause the point where the plasma intercepts the target to move back and forth along the target, but the relatively small modulation of the coil currents will not produce a large change in average heat loading.

Of the factors outlined above an increase in the core radiation fraction and inclining the divertor target are obvious candidates as means to reduce the peak heat load. An inclination of 8° coupled with an f_{RAD} of 0.75 will reduce the peak target heat flux to ~ 30 MW/m^2, which is still above the allowable levels described in Sec. 6.5. The possibility of impurity injection to radiate within the divertor plasma, therefore, is considered.

6.3.3. Impurity Radiation in the Divertor

A simple analytic model has been developed to make an initial assessment of the feasibility of the approach to reduce the divertor target heat load by injecting high Z impurities into the divertor plasma. The basic idea is to inject a high Z gas, such as Xenon, into the divertor plasma upstream of the target but downstream of the null-point or throat. The impurity should then be distributed over the plasma downstream of the injection point but should be impeded from flowing upstream towards the core plasma by the strong frictional force imposed by the background plasma.

The basis of the model is similar to that used in reference [15]. Power flow along the field line is assumed to be purely by electron conduction

$$q_{\|} = -K_o T^{5/2} \frac{dT}{dz} \qquad (6.3.-2)$$

where $q_{\|}$ is the parallel heat flux, $K_o T^{5/2}$ is the Spitzer value for the electron

thermal conductivity, T is the electron temperature and z is the direction along the field line. Power radiated by the impurities reduces the parallel heat flux

$$\frac{dq_{||}}{dz} = - P_{RAD} = - n_e n_I L(T) \qquad (6.3.-3)$$

where P_{RAD} is the power radiated per unit volume of plasma, n_e is the electron density, n_I is the impurity ion density and L(T) is the radiative cooling rate for the impurity ion. Further assumptions are that the electron pressure, p ($\equiv n_e T$), and the impurity fraction, f_I ($\equiv n_I/n_e$), remain constant. Under these conditions,

$$\frac{dq_{||}}{dz} = - p^2 f_I \frac{L(T)}{T^2} \qquad (6.3.-4)$$

Post [16] has given analytic fits to L(T) for various impurities in coronal equilibrium at higher temperatures (T > 80 eV for Xenon), but data for L(T) are virtually non-existent for high Z impurities at low plasma temperatures. To overcome this problem, it is assumed that the radiative cooling rate varies as follows with some power of the temperature

$$L(T) = L_0 T^{\alpha} \qquad (6.3.-5)$$

for temperatures below the cut-off point given in Ref. [16]. As there is such a large uncertainty in the radiation data the rather poor assumption of coronal equilibrium, as the residence time of the impurity ion is too short for the equilibrium concentrations of the various ionization states to be reached, is not significant. It should also be emphasized that any conclusions are subject to this same uncertainty.

With these assumptions an analytic solution to the equations can be obtained if all of the divertor power is radiated, i.e. $q_{||} = 0$ and $T = 0$ at the divertor target. Fig. 6.3.-5 shows the fractional impurity concentration as a function of the core plasma radiation fraction, f_{RAD}, for two values of α, 0 and 2. The first case, $\alpha = 0$, corresponds to a constant L(T) at low temperatures;

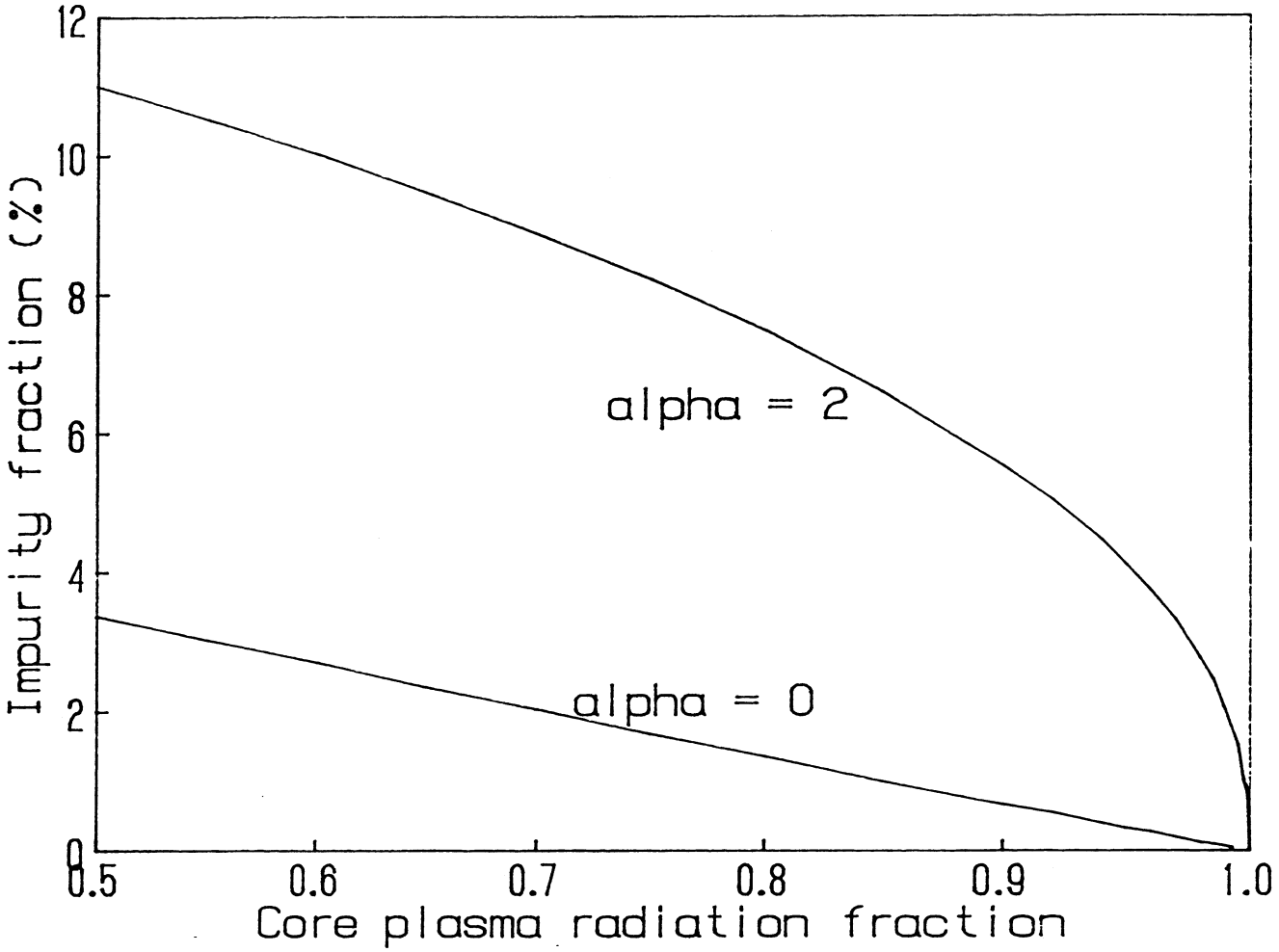

Fig. 6.3.-5. Variation of fractional impurity concentration with f_{RAD} for two values of the radiation parameter α (α = 0 and 2).

for the other case L(T) varies as T^2 at low temperatures. It is known that at very low temperatures (well below the ionization energy i.e. $T \leq 5$ eV) L(T) must fall, but it will probably remain relatively high at higher temperatures. The case for $\alpha = 0$, therefore, is likely to be more realistic except at the lowest temperatures. The figure shows that a fractional impurity concentration of the order of a few per cent is necessary to radiate all the divertor power.

The main aim of injecting impurities is to spread the heat load over a large area. Fig. 6.3.-6 shows the normalized radiated power profile along the plasma for the two values of α. For $\alpha = 2$ the radiated power is constant; this is clear from equation (6.3.-4). For $\alpha = 0$, the radiated power rises rapidly towards the end of the field line, with a singularity at the target, which can also be explained from equation (6.3.-5); for constant L(T) the radiated power becomes infinite at $T = 0$. This behaviour is clearly unphysical because, as explained earlier, L(T) must fall at very low temperatures. It would be possible to solve the set of equations numerically with a more realistic expression for L(T), but the approximations and assumptions in the model make such a detailed solution inappropriate. The solution obtained, therefore, is cut off somewhat arbitrarily at a point close to the target, the point where the temperature has fallen to 10 eV being chosen here. This cut-off still leaves a large peaking factor in the radiated power profile, implying that the objective of spreading the heat load as uniformly as possible over the whole divertor wall area has not been achieved to a satisfactory extent.

To convert these profiles of plasma radiated power to heat flux distributions on the divertor surfaces, an integration package has been written. The plasma is treated as a line radiation source located between two surfaces, with uniformity in the third dimension assumed, as illustrated in Fig. 6.3.-7. The heat load at any point on the plate is obtained by integrating the contribution from each element of the plasma.

Figures 6.3.-8 and 6.3.-9 present the results for the two cases ($\alpha = 0$ and 2) in the form of a peaking factor for the heat flux, a value of 1 representing a perfectly uniform power deposition on the surfaces. For $\alpha = 0$, the top surface, which is further away from the plasma, sees a relatively low and smoothly distributed heat flux, but a large peaking factor is predicted for the bottom surface. The size of the peak is strongly dependent on the position of the cut-off point for the radiated power profile, but the width of the peak is fairly constant at about 1 - 2 cm for a peaking factor of 5. For $\alpha = 2$ the heat

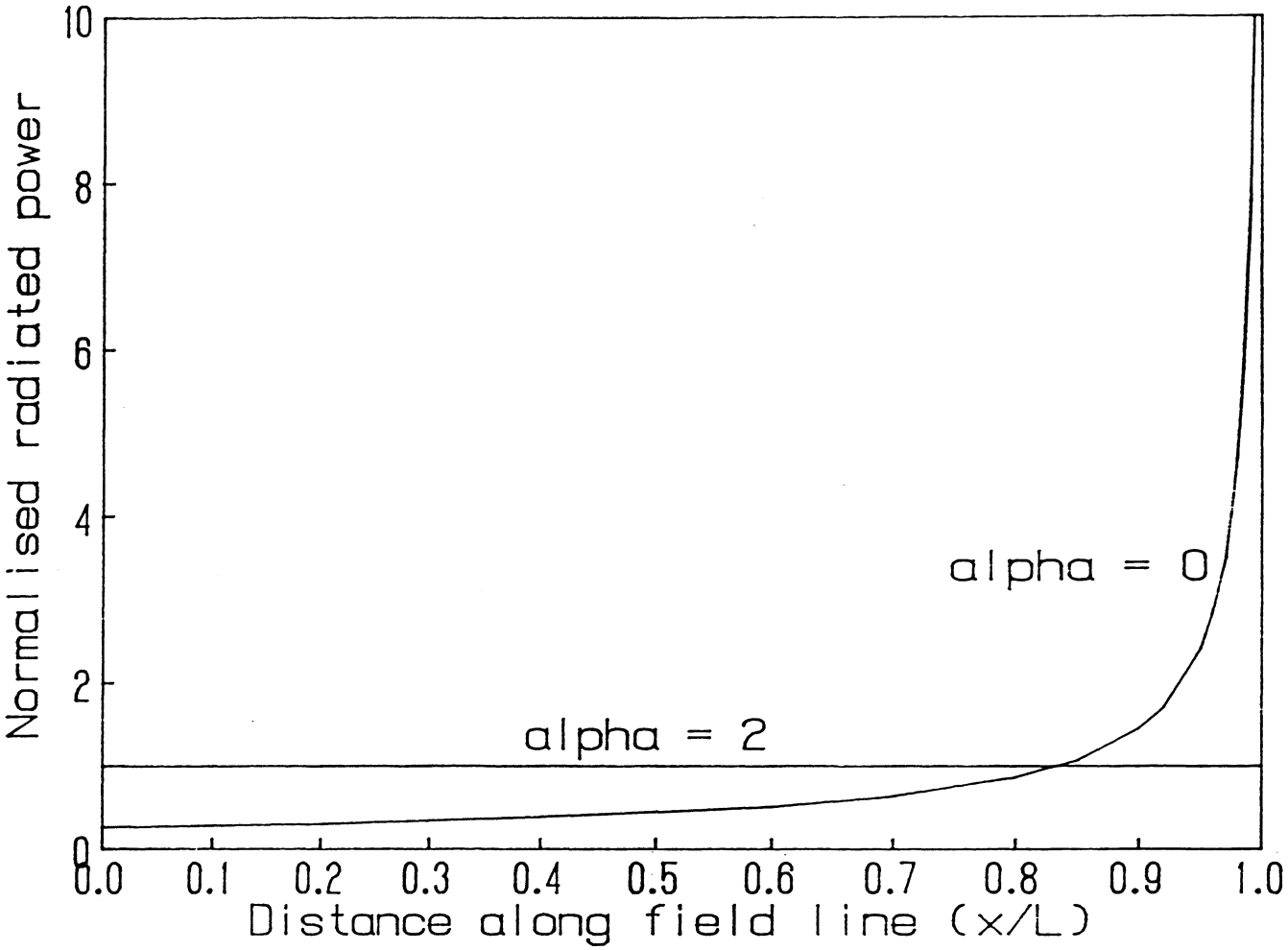

Fig. 6.3.-6. Variation of the normalized radiated power in the plasma with axial position along the field line for two values of the radiation parameter α (α = 0 and 2).

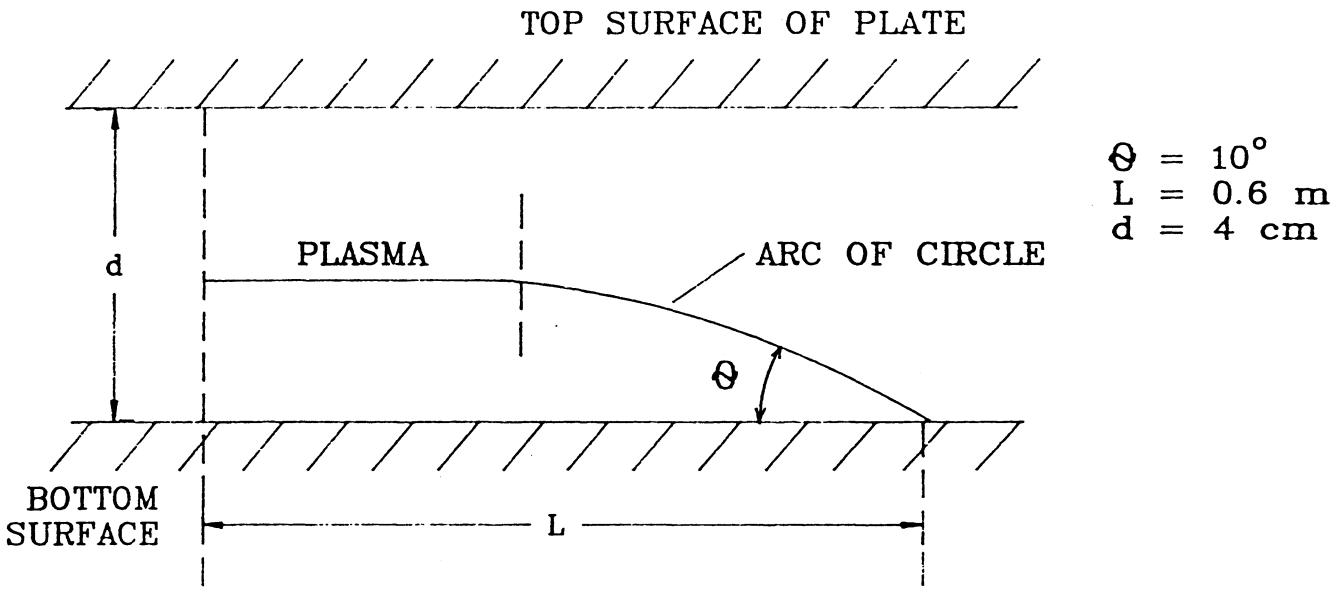

Fig. 6.3.-7. Geometry used in estimating distribution of heat flux on divertor plate.

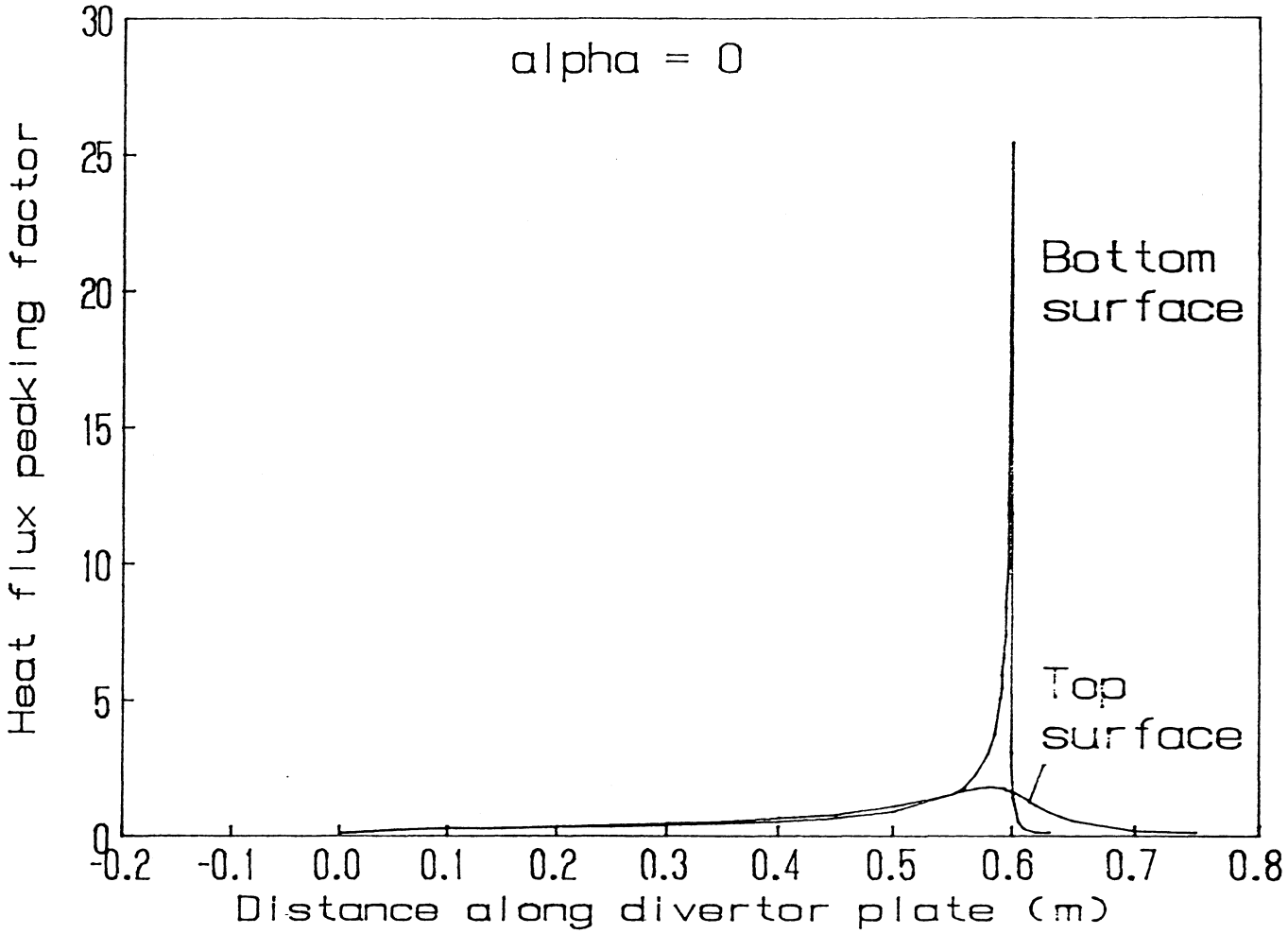

Fig. 6.3.-8. Heat flux distribution along divertor plate for case when the radiation parameter $\alpha = 0$.

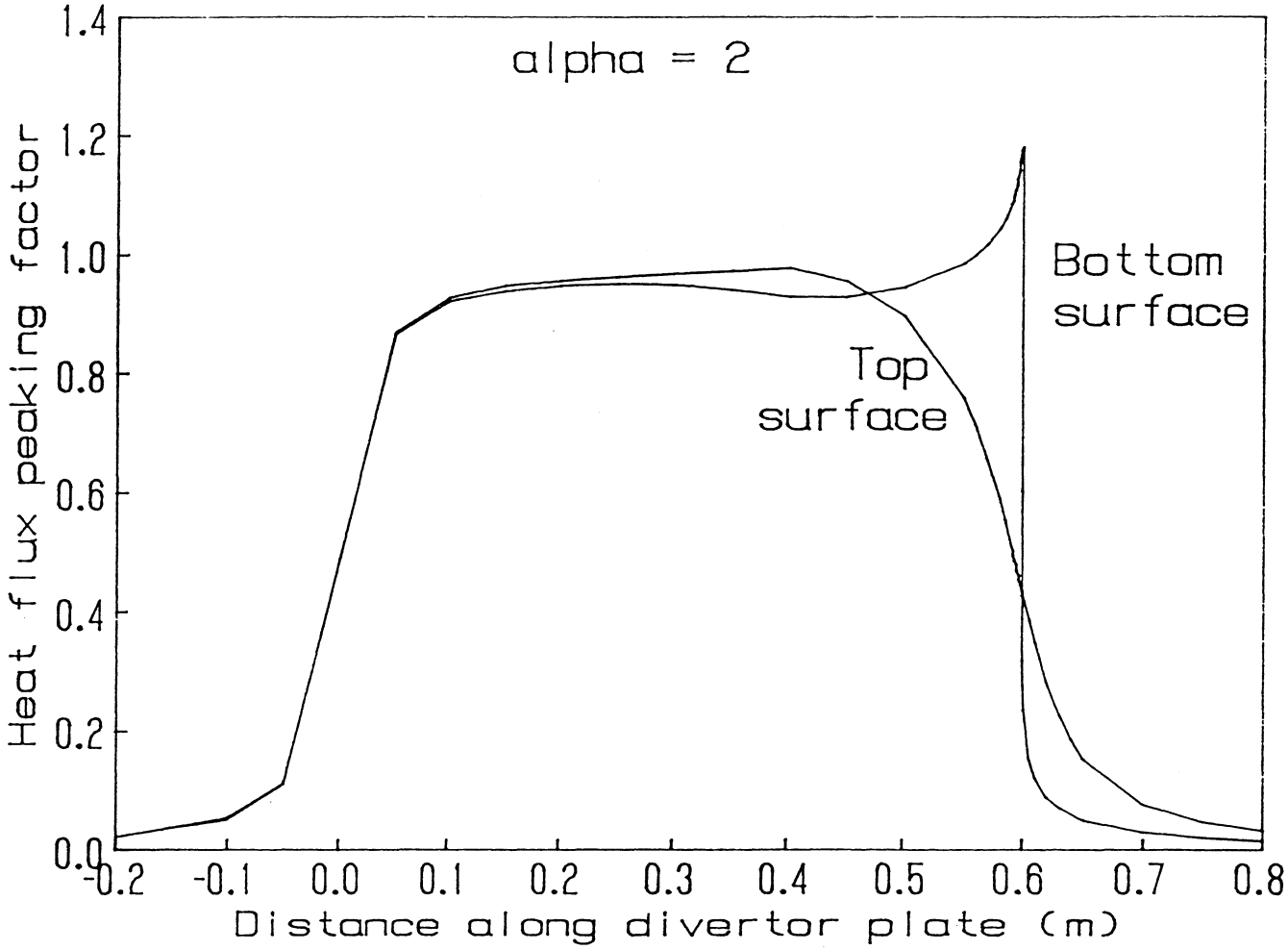

Fig. 6.3.-9. Heat flux distribution along divertor plate for case when the radiation parameter $\alpha = 2$.

flux varies smoothly along the surface except for a small peak where the plasma intercepts the target.

Future modeling will remove the unphysical singularities in the heat flux which arise from the simplified form for L(T) and the treatment of the plasma as a line source of radiation instead of a distributed source. Another modification will be to include a fraction of the power being transported to the target by particles, as it is not realistic to assume that all the power can be radiated.

A major consideration in assessing the feasibility of impurity injection to radiate the divertor power is whether the impurities remain confined in the divertor. As the high Z impurity concentration in the divertor plasma must be ≤ 1 %, while in the core plasma it should be ≤ 0.01 % (Sec. 4.7.2), a very efficient mechanism is required for retaining impurities within the divertor. The "closed" magnetic configuration of the RFP toroidal divertor is of value in this respect, as the divertor chamber can be effectively separated from the main plasma chamber by only a narrow plasma channel. This decoupling is not possible in a tokamak with a poloidal divertor generated by external PF coils; in this case there is no separate divertor chamber and a greater tendency exists for neutral gas to leak from the divertor towards the main plasma.

The forces acting on an impurity ion in a background plasma have been considered by Neuhauser [17], using a test particle approach. There is a strong frictional force which tends to drag the impurity along with the background plasma but also a thermal force pointing in the direction of increasing temperature. An electrostatic force arising from the ambipolar electric field also exists and there may be other forces due to variations in the magnetic field strength.

For impurities in a high charge state the first two forces tend to dominate except near the target where electric fields may be important. Neuhauser has identified the following criterion, which when satisfied implies that highly charged impurities tend to be entrained and drift with the background plasma flow:

$$M > \frac{\lambda_I}{\lambda_T} \qquad (6.3.-6)$$

where M is the Mach number of the drifting plasma, λ_I is the mean free path for

Coulomb collisions between impurity ions and the background plasma ions and λ_T is the axial scale length for the ion temperature.

The density and temperature profiles obtained with the simple impurity radiation model indicate that Mach numbers of the order of 0.1 are required to satisfy the criterion. For the high-recycling conditions expected in the divertor, however, the plasma flow will tend to stagnate upstream of the ionization zone and it is unlikely that a sufficiently high Mach number will be achieved except in the region close to the target. As the impurities will be injected far upstream of the target, near the throat of the divertor, the criterion implies that the impurities will be driven up the temperature gradient against the background plasma flow towards the core plasma. This conclusion is preliminary, however, and further work on the plasma flows and on the impurity transport is being undertaken.

An extra complication arises when two-dimensional simulations of the scrape-off layer plasma are examined. A number of these models have shown that the background plasma flow itself can reverse over a portion of the scrape-off layer such that it is flowing away from the divertor target [18-20]. If this flow reversal occurs in TITAN then it would seriously impact the viability of the proposed impurity injection technique. Plans for more detailed modeling of the edge-plasma during the next phase of the TITAN project, including a study of these effects, are discussed in the next section.

6.3.4. Future Edge-Plasma Modeling

6.3.4.1. First Wall and Divertor Erosion

First wall and divertor erosion rates for TITAN will be estimated by coupling the ODESSA plasma edge transport code to either the FENAT [21] or SPUDNUT [22] (or both) neutral particle transport codes. Although computationally fast, SPUDNUT has the disadvantage of being one-dimensional and uses an approximate ion distribution function for generating charge-exchange neutrals, whereas FENAT is a 2-D finite element code that uses a local Maxwellian distribution for the ions but is based on approximate diffusion theory, is slower than SPUDNUT and presents greater interfacing difficulties with ODESSA. Recent numerical results indicate that the plasma temperature adjacent to the first wall (5 cm from the separatrix) is in the range 30 - 50 eV, suggesting that a substantial contribution from ion sputtering may be anticipated especially under high divertor recycling conditions. The

dependence of erosion rates on the radiation fraction and the scrape-off layer width will be investigated.

6.3.4.2. Self-Consistent Plasma and Neutral Particle Transport

Under the high recycling conditions that are desirable for operation, the plasma flow in the scrape-off layer may reverse locally if the recycling coefficient locally exceeds unity. This happens because recycling neutrals do not ionize at the same radial location at which they were born. The flow of particles is consequently out of the divertor at certain radial locations, although the integrated or net flow into the divertor must be positive and equal to the core efflux. If this flow reversal occurs, it will have serious implications for the feasibility of radiatively cooling the divertor plasma as the impurities will no longer be confined within the divertor.

The simulation of this effect requires accurate modeling of neutral particle transport in the divertor. In the longer term, a Monte Carlo code will be used to carry out the simulation in three dimensions using an accurate representation of the geometry of the divertor and the pumping ducts. In the near future, however, for computational expediency, a simplified model will be developed that will be fully implicit with ODESSA while retaining the essential non-local effects that may drive flow reversal.

6.3.4.3. Coupling of Core and Edge-Plasma Models

All calculations using ODESSA thus far have been performed with prescribed particle and heat fluxes at the separatrix. These boundary conditions are supposed to be a measure of core particle and energy outfluxes. While this approach is reasonable for the heat flux (because there is little energy recycling between core and edge), the significant stalling and even reversal of particle flow at or near the separatrix that occurs under high divertor recycling conditions makes it difficult to prescribe the particle flux at the separatrix with any accuracy. This approach nevertheless is universally adopted in edge-plasma modeling [18,19] and is not restricted to ODESSA. To circumvent this shortcoming, a combined core-edge transport calculation will be carried out by coupling ODESSA to the RFP core transport code described in Sec. 4.6. The particle flux will then be self-consistent with the recycling in the divertor and, hence, the core particle confinement time will be a function of the recycling coefficient. Incorporation of this effect is expected to have an important impact on the ash exhaust.

6.3.4.4. Axial Resolution of the Edge-Plasma

A one-dimensional, axial (along magnetic field lines) code, known as ZCODE, will be used to resolve issues associated with the strongly varying plasma density and temperature along a diverted field line. The model is based on a two-fluid plasma description and includes impurity radiation based on coronal equilibrium and a one-dimensional neutral atom transport model (SPUDNUT) for recycling at the divertor target. In addition, the expansion and contraction of field line bundles is included since it can concentrate the heat and particle loads by a substantial factor (Sec. 6.2.4). Physical sputtering at the divertor plate due to plasma and charge-exchange neutral particles is calculated and the code checks for frictional entrainment by impurities. The heat load on the divertor plate due to radiation and plasma bombardment is also evaluated. These effects have been identified as crucial issues for the TITAN divertor design.

6.4. DIVERTOR AND FIRST WALL HEAT LOADS

The divertor configuration [5] shown in Fig. 6.4.-1 is used to formulate an expression for the peak heat load in the divertor chamber in order to identify high-leverage variables which could affect a reduction in the peak heat load below the design constraint of $q_D \simeq 5$ MW/m^2. The peak heat load is simply the ratio of the power entering the divertor and the available surface area multiplied by a peaking factor. Specifically,

$$q_D = \frac{(1 - f_{RAD})\, P_{TR}\, f_{PK}}{N_D A_D} , \qquad (6.4.-1)$$

where $P_{TR} = P_\alpha + P_\Omega$ represents the total steady state plasma heating power (i.e., alpha-particle, P_α, and Ohmic, P_Ω, powers), f_{RAD} is the fraction of the transport power radiated (uniformly) to the first wall, f_{PK} is a peaking factor applied to the divertor chamber/plate region, N_D is the number of divertors, and A_D is the area available within a divertor for the absorption of the radiated and convected power. The divertor surface area is theoretically limited to a maximum of four times the annular cross-sectional area bounded by the first-wall and outer blanket/shield radii to prevent interference with either the plasma or the poloidal-field coils, under the assumption that one side of each of four annular discs enclosing the divertor flux bundle, as shown in Fig. 6.4.-2, form

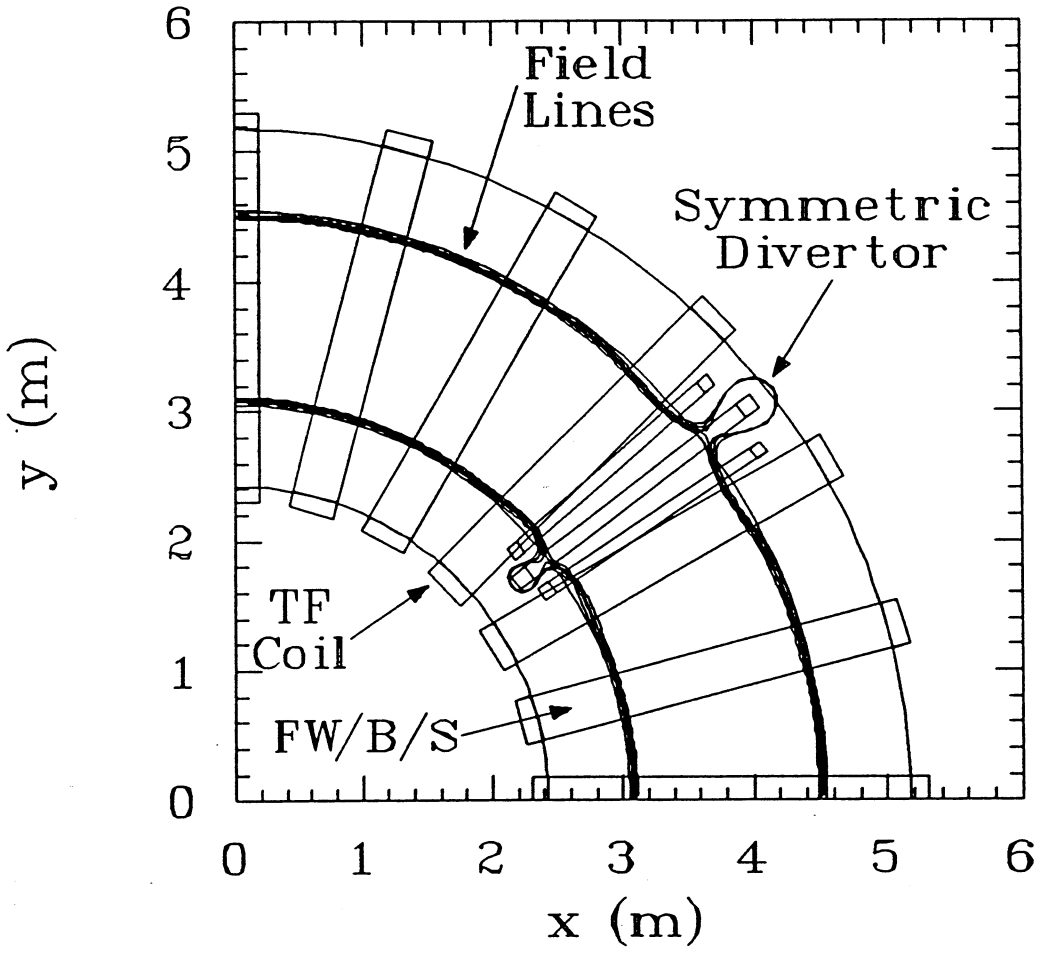

Fig. 6.4.-1. An equatorial-plane view of a quadrant of the CRFPR divertor design [5].

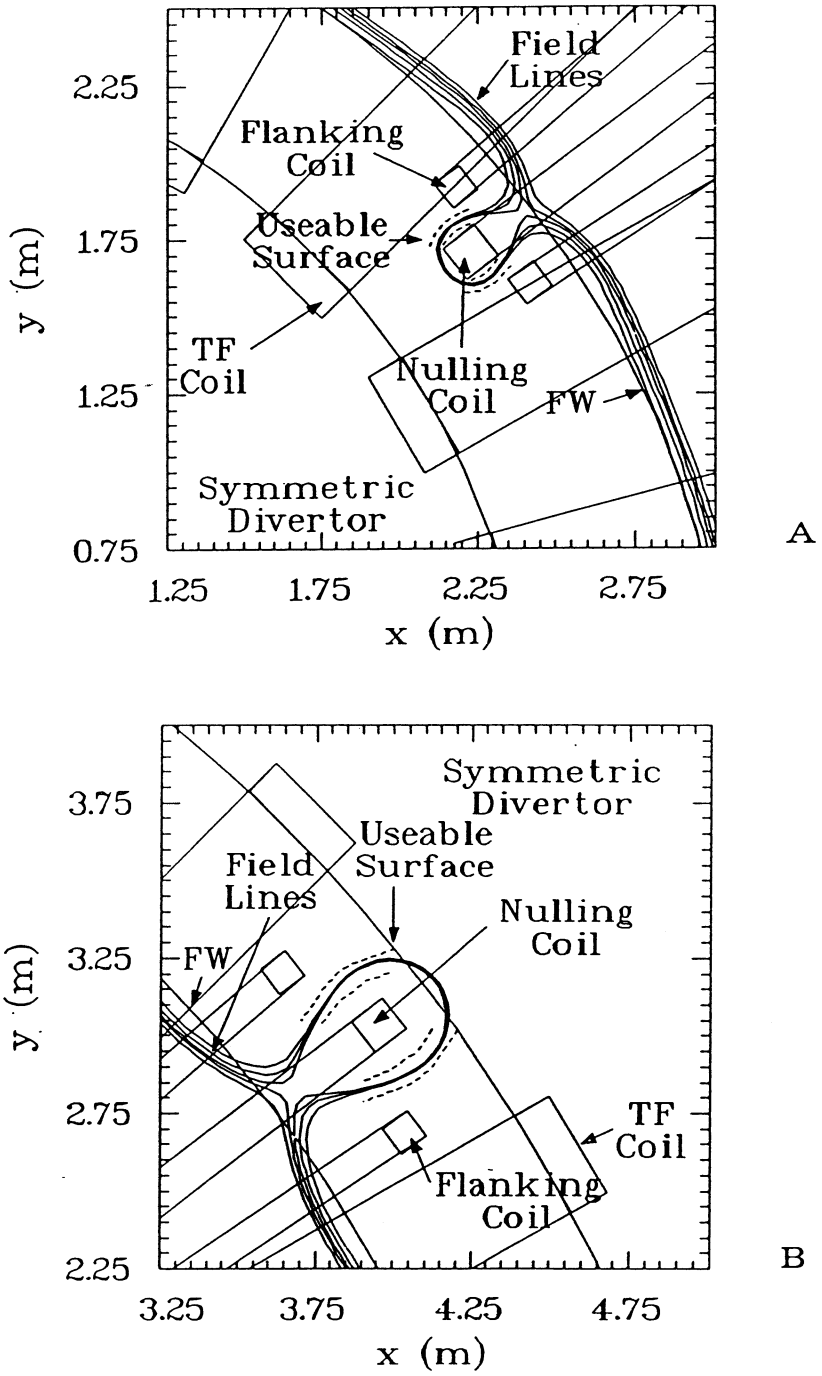

Fig. 6.4.-2. An enlargement of the inboard (A) and outboard (B) location of the divertor in the equatorial plane. Also shown are the useable surfaces for absorbing the power entering the divertors and then being radiated.

this idealized divertor chamber. In practice, the divertor surface area is less than this limit by a factor $f < 0.5$ because of inboard versus outboard asymmetries. The entrainment of radiating high Z impurities within the divertor plasma has been assumed here, but if impurities are not entrained then the divertor surface area is reduced to just the target area, resulting in $f < 0.1$. Hence,

$$A_D = 8\pi(r_w + \Delta b/2)\, f\Delta b, \qquad (6.4.-2)$$

where r_w is the first-wall minor radius, and Δb is the annular thickness of the first wall/blanket/shield.

In order to maintain the toroidal-field ripple below the 0.3% design value [4], the number of toroidal-field coils (TFCs), N_{TF}, should scale approximately linearly with aspect ratio, $A \equiv R_T/r_p = R_T/r_w x$, where $x \equiv r_p/r_w$ and r_p is the plasma minor radius. Furthermore, in order to preserve the fraction, f_B, of the blanket displaced by divertors as N_{TF} varies, the number of divertors, N_D, scales linearly with N_{TF}. Normalizing to an earlier divertor design [5] ($A = 5.35$, $N_{TF} = 24$, $N_D = 4$), the following scaling relationship holds:

$$N_D = 4.48\, A\, R_N\ , \qquad (6.4.-3)$$

where $R_N = N_D/N_{TF}$. A divertor for the earlier design [5] occupies sixty percent of the volume between TFCs; hence, the blanket-loss fraction is $f_B = 0.6R_N$. Furthermore, the first-wall radius can be derived from the neutron wall loading, $I_w(MW/m^2)$, as follows:

$$r_w = [P_{TR}/\pi^2 I_w A x(1 + 5/Q_p)]^{1/2}, \qquad (6.4.-4)$$

where $Q_P \equiv P_F/(P_\Omega + P_{AUX})$ and P_F is the total fusion power. The following design equation results upon substituting Eqs. (6.4.-2) - (6.4.-4) into Eq. (6.4.-1),

$$q_D = \frac{0.0089(1 - f_{RAD})P_{TR}f_{PK}}{R_N A f \Delta b([P_{TR}/I_w A x(1 + 5/Q_p)]^{1/2}/\pi + \Delta b/2)} . \qquad (6.4.-5)$$

where f is the fraction of the total divertor surface area available for heat recovery. Similarly the heat load on the first wall is given by

$$q_{FW} = f_{RAD}\, I_w(1 + 5/Q_p)/4 . \qquad (6.4.-6)$$

Values for the variables appearing in Eqs. (6.4.-5) and (6.4.-6) that are consistent with the design points described in Sec. 5.3.2. are listed in Table 6.4.-I. The value for f is based on the sketches of divertor surfaces shown in Fig. 6.4.-2. The useable surfaces do not extend radially inward to the first wall because two mechanisms assumed to confine the radiating impurities, mirror confinement and frictional entrainment, are active only near the divertor plate. The confining weak field mirrors (mirror ratio, $M \leq 1.5$) are located approximately where the field lines entering the divertor chamber from the plasma "bunch" together. Frictional entrainment of impurities by plasma flow is most effective in flows with high Mach number, which occurs near the divertor plate. The latter confinement mechanism provides the stronger confinement.

TABLE 6.4.-I
Typical TITAN Divertor Parameters

Parameter	Value
Transport power, P_{TR}(MW)	500.
FW/B/S thickness, Δb(m)	0.775
Useable fraction of divertor surface area, f	0.4
Heat load peaking factor, f_{PK}	2
Ratio of plasma to first-wall radii, $x = r_p/r_w$	0.92
Ratio of fusion to heating powers, Q_p	281
Neutron wall loading, I_w(MW/m^2)	10, 18
Plasma aspect ratio, A	6.5, 8.5
Ratio of divertors to TFCs, R_N	1/6, 1/4
Radiation fraction, f_{RAD}	0-1

Since a low value of f is assumed, only modest peaking of the heat load is assumed for a given value of $q_D(MW/m^2)$. Future efforts will concentrate on the accurate determination of f_{PK} due to such effects as poloidal asymmetries and flux surface expansion or contraction. A value of x = 0.92 is consistent with an 0.05 m thick scrapeoff used for the 18-MW/m^2 Strawman design (see Sec. 5.3.2), and the Q_p for the 18-MW/m^2 Strawman design (Sec. 5.3.2) has been assumed. Two representative sets of I_w, A, and R_N values were considered and represent a reasonable range for those TITAN design parameters to lower q_D. It should be noted that R_N = 1/6 was used for the CRFPR [5], with R_N = 1/6 and 1/4 corresponding to f_B = 0.10 and 0.15, respectively. The radiation fraction was parametrically varied over the range $0 \leq f_{RAD} \leq 1$.

The results of the parametric evaluation of Eqs. (6.4.-5) and (6.4.-6) are shown in Fig. 6.4.-3. The variable exerting the highest leverage upon q_D, is f_{RAD}, followed in decreasing order of importance by R_N, A, and I_w. The relative insensitivity of heat flux to neutron wall loading is a result of the assumption of fixed blanket/shield thickness, which is the main factor in determining the divertor surface area. Only the variable f_{RAD} can be adjusted independently to yield $q_D \leq 5$ MW/m^2. For the 18-MW/m^2 Strawman design with a nominal R_N = 1/6, an $f_{RAD} \geq 0.8$ is required to satisfy the 5-MW/m^2 heat load constraint. Lowering the neutron wall loading to 10 MW/m^2 or raising the aspect ratio to 8.5 and simultaneously satisfying the 5-MW/m^2 heat load constraint would permit a reduction in f_{RAD} to 0.76. Increasing R_N to 1/4 would yield a larger reduction in f_{RAD} to 0.7 and satisfy the 5-MW/m^2 heat load constraint. If $f_{RAD} < 0.6$ is more reasonable from a physics viewpoint, then R_N, A, and I_w must be adjusted simultaneously to 1/4, 8.5, and 10 MW/m^2, respectively, in order to hold q_D below ~ 5 MW/m^2. These values of R_N, A, and I_w would adversely affect tritium breeding, plasma confinement, and the efficacy of single-piece FPC maintenance. From an engineering viewpoint, it is desirable to have the first wall and divertor at the same heat load and, therefore, similar thermal stress, which would necessitate f_{RAD} ~ 0.75-0.9. Finally, it is recommended that future design efforts focus on a design with I_w = 18 MW/m^2, A = 6.5, R_N = 1/6, and $f_{RAD} \geq 0.8$.

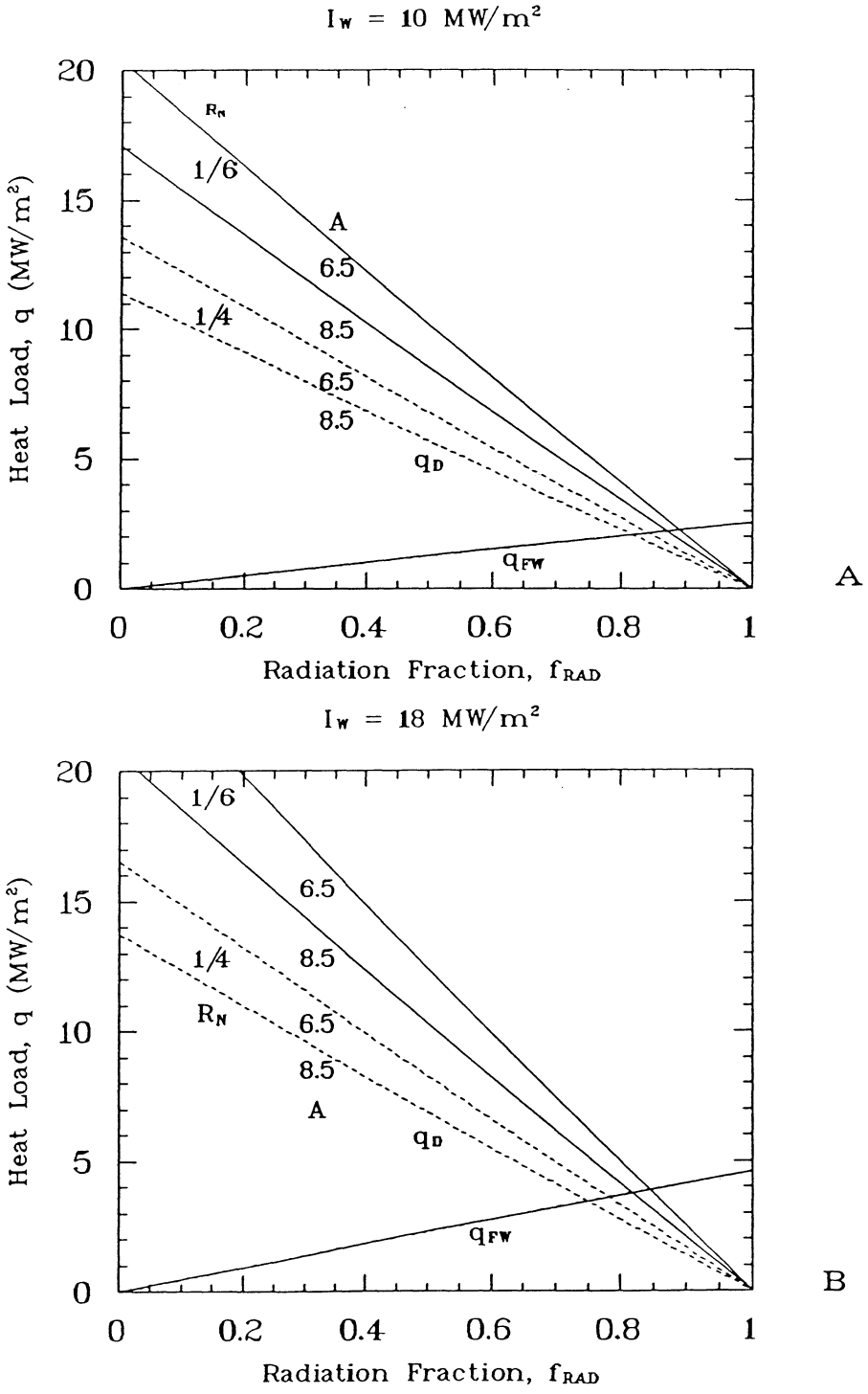

Fig. 6.4.-3. The heat load in the divertor, q_D, and on the first wall, q_{FW}, as a function of radiation fraction for various plasma-aspect ratios and the ratio of divertors to TFCs for the 10-MW/m² Strawman design (A) and the 18-MW/m² Strawman design (B).

6.5. DIVERTOR COOLING

Several options have been considered for divertor cooling for TITAN. For the Li/V blanket concept, liquid metal cooling is attractive for reasons of compatibility with the overall design; this option is considered in Sec. 6.5.1. Water is an obvious candidate as a coolant for high-heat-flux components and is particularly suitable for use in conjunction with the water-cooled blanket (Sec. 6.5.2). Safety considerations, however, preclude the use of a water-cooled divertor in a design with a blanket containing liquid lithium. Helium cooling of the divertor is compatible with any of the blanket concepts considered and a study of this approach is described in Sec. 6.5.3. Finally, various innovative cooling concepts are considered in Sec. 6.5.4.

6.5.1. Liquid Metal Cooling

6.5.1.1. Introduction

A preliminary study of liquid metal cooling of the divertor has been made using either lithium or sodium cooling. Of all the liquid metals, Li and Na have the most favorable thermal properties such as large specific heat, which is very important in high-heat-flux applications. In using electrically conducting liquid metals in a fusion reactor environment, coolant pressure and pumping power due to the magneto-hydrodynamic effect are important. Because of the limitation on the maximum temperature of the structural material, it is advantageous to design for turbulent flow in the coolant channels to reduce the film temperature drop. As the heat flux on the divertor surfaces is predicted to be high, it may be necessary for the coolant channel walls to be electrically insulated to avoid incurring a prohibitively high coolant pressure drop. Such electrical insulation is not necessary for the first wall coolant tubes where the heat flux is somewhat lower and the magnetic field strength in the direction normal to the coolant flow is lower.

In this preliminary study, three cases have been examined for both Li and Na. These are: (a) laminar flow without insulation, (b) laminar flow with the channel walls electrically insulated, and (c) turbulent flow with the channel walls insulated. In the next section, the possible coolant channel configurations are discussed and the results of MHD and thermal hydraulic calculations are presented. Some design conclusions are drawn in Sec. 6.5.1.3.

6.5.1.2. Results

Figure 6.5.-1 shows possible arrangements of the coolant channels and the directions and the approximate magnitudes of the magnetic fields. In case (a), the channels run along the poloidal direction, parallel to the dominant magnetic field. In cases (b) and (c), the coolant channels run perpendicular to the dominant magnetic field. In case (b), the desired coolant exit temperature can be obtained by adjusting the length between inlet and outlet. Only one pass across the magnetic field occurs in case (c). The exit temperature will be low in this case unless the coolant velocity is very small. Because of the much higher coolant velocity for turbulent flow and the resulting large MHD pressure drop in cases (b) and (c), only case (a) has been selected for this study.

The following results are for the 18 MW/m^2 neutron wall loading design. It is assumed that there are four divertors each with 10.4 m^2 cooling surface area. Vanadium alloy coolant tubes with inside diameter of 8 mm and wall thickness of 1 mm have been used. Inlet temperatures for Li and Na are 300 °C and 200 °C, respectively. The allowable maximum coolant exit temperature is determined such that the outer surface tube wall temperature does not exceed 750 °C. The total pressure drop includes both MHD and friction pressure losses when the tube wall is not electrically insulated, whereas only the friction pressure loss occurs when the tube wall is electrically insulated. The pressure drop does not include any loss due to bends, inlet/outlet effect, variations in the magnetic field along the inlet/outlet ducts, etc. as the detailed coolant-tube configurations are not decided at this stage. The equations for MHD and friction pressure drops are given in Table 8.4.-I (Section 8). Thermal analyses in the tube wall and in the coolant for calculating the wall and film temperature drops are similar to those presented in Section 8.

Figures 6.5.-2 and 6.5.-3 show the results for laminar flow without and with electrically insulated tube walls respectively. Both of these figures show that, for laminar flow, the limiting factor is the wall temperature, even though insulating the wall almost eliminates the MHD pressure drop. The maximum cooling capability with laminar flow for both Li and Na appears to be about 3 MW/m^2 without insulation and about 3.5 MW/m^2 with insulation. The limiting factor is the high coolant pressure and the resulting high primary stress. The assumed primary design stress limit of 100 MPa is reached at a coolant pressure of about 25 MPa.

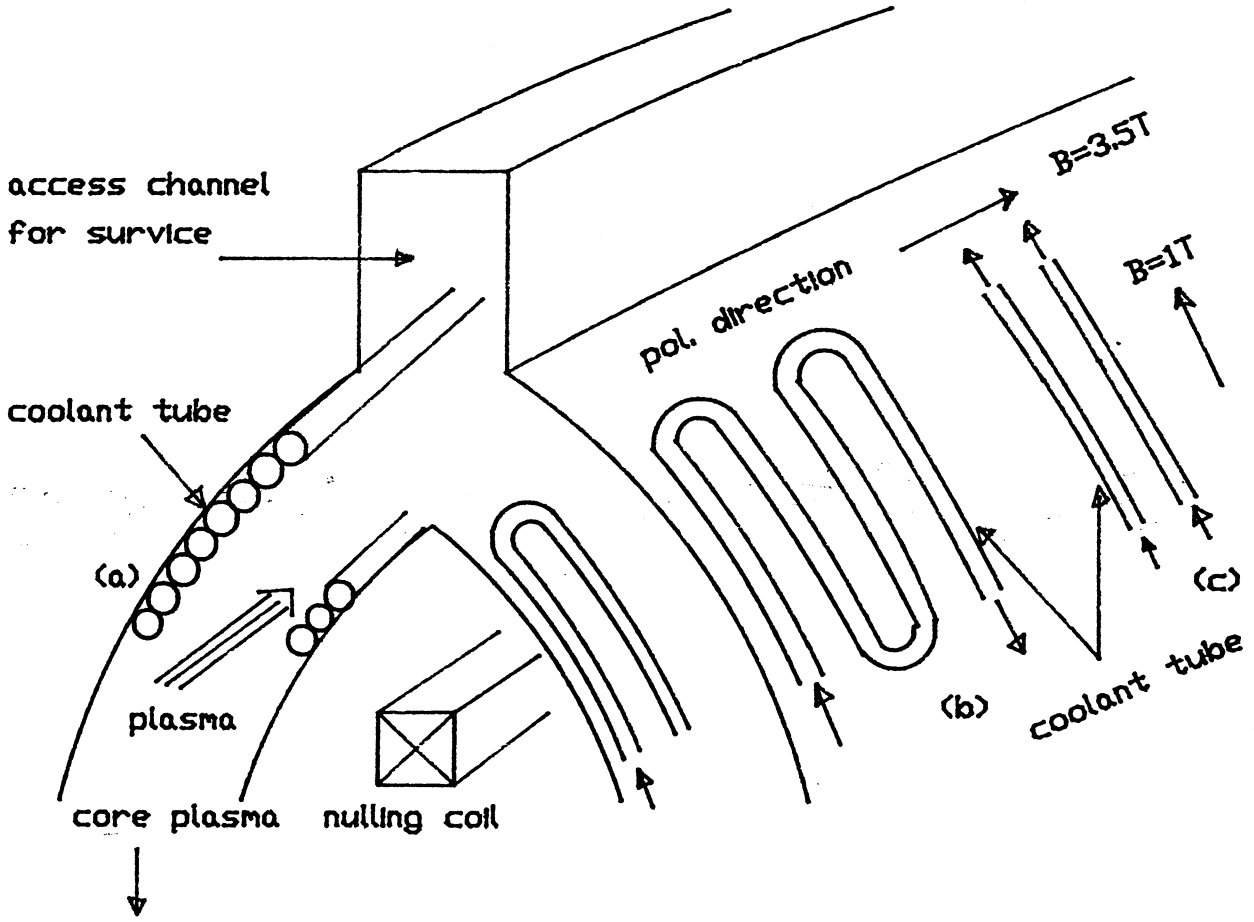

Fig. 6.5.-1. Possible configurations of cooling tubes for divertor cooling. The coolant tubes can be arranged along the poloidal direction as in case (a), normal to the poloidal direction with multiple passes as in case (b), or normal to the poloidal direction wtih a single pass as in case (c).

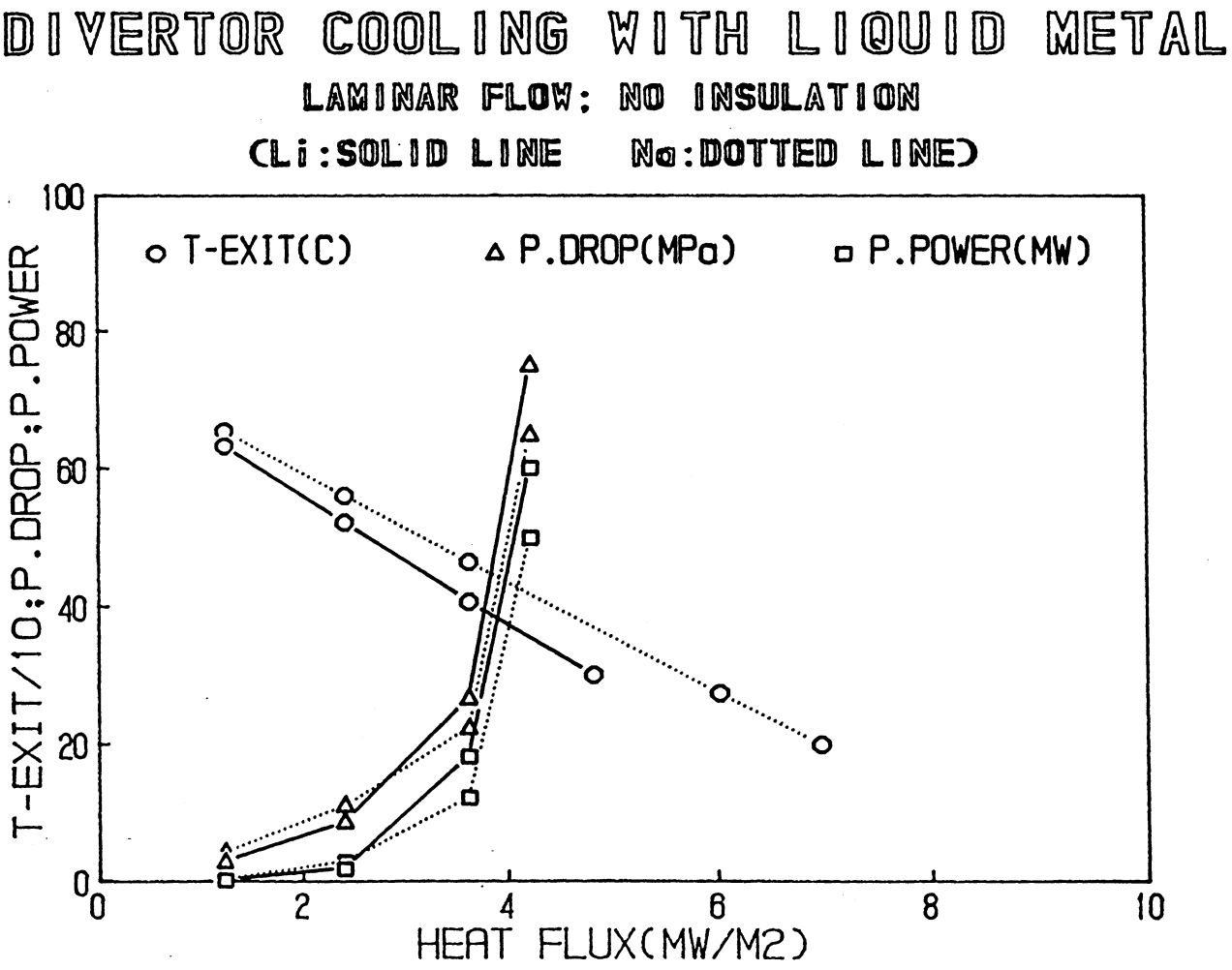

Fig. 6.5.-2. Variation of coolant exit temperature, pressure drop and pumping power with f_{RAD} or surface heat flux. The flow is laminar and the tubes are not electrically insulated.

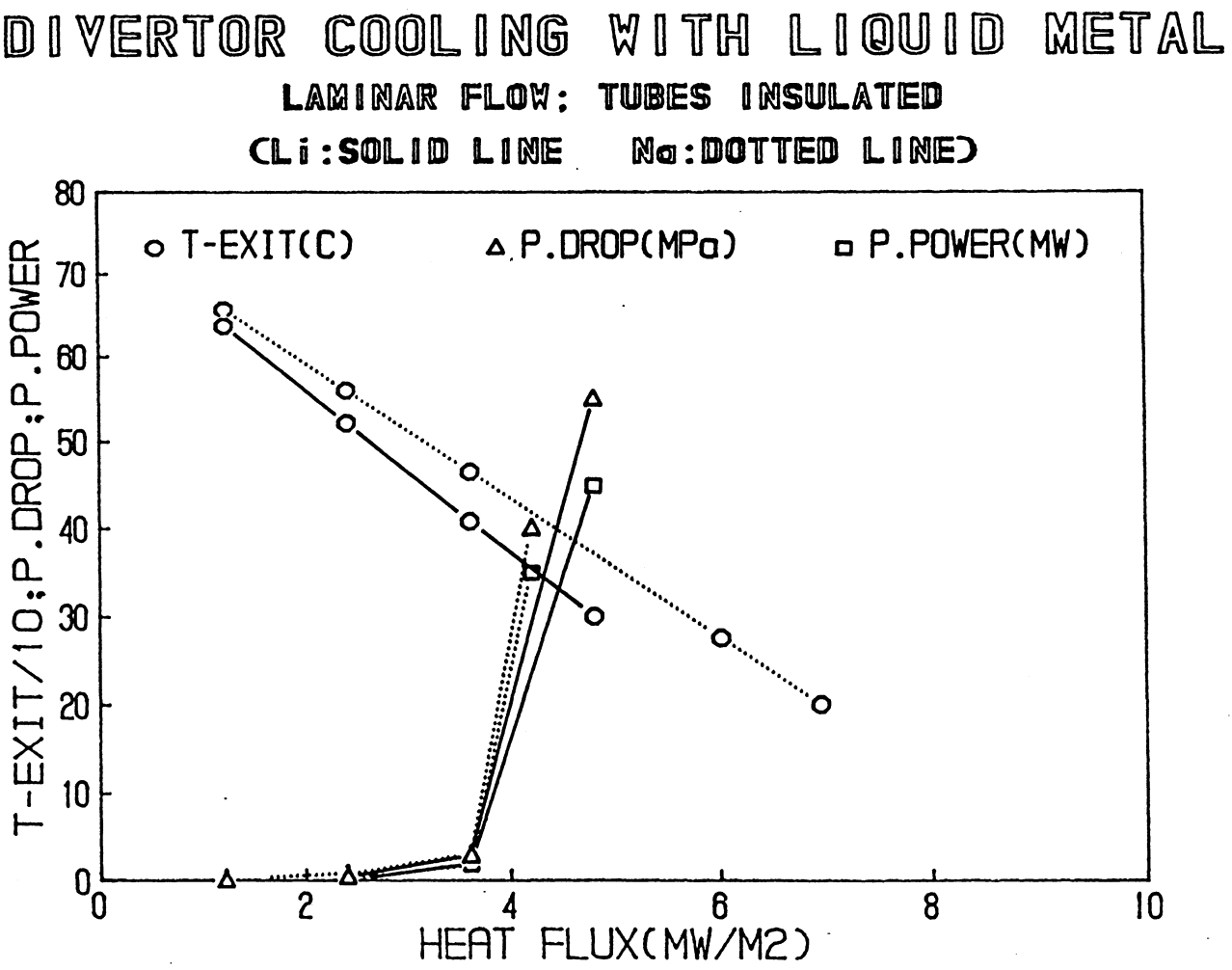

Fig. 6.5.-3. Variation of coolant exit temperature, pressure drop and pumping power with f_{RAD} or surface heat flux. The flow is laminar and the tubes are electrically insulated.

Figure 6.5.-4 shows the results with turbulent flow with the tube wall electrically insulated. The minimum velocity for turbulent flow is calculated by equating the Reynolds number to the larger of 500 $H_{\perp}$ and 60 $H_{\parallel}$ where $H_{\perp}$ and $H_{\parallel}$ are the perpendicular and parallel Hartmann numbers, respectively. For the present case, the minimum velocity for turbulent flow is 33 m/s for Li and 17.6 m/s for Na. It is assumed that the coolant flows only one complete poloidal turn around the plasma. With turbulent flow and one complete turn, Figure 6.5.-4 shows that the maximum heat flux capabilities of Li and Na are about 7 MW/m^2 and about 4 MW/m^2 respectively. Using partial turns at high heat fluxes, a maximum heat flux capability of about 9 MW/m^2 can be reached for both Li and Na. The pumping power and coolant pressure are of the order of a few MW and below 5 MPa respectively.

6.5.1.3. Conclusions

Divertor cooling using liquid metal is feasible if the coolant tubes are electrically insulated and if the flow is turbulent. Liquid metal cooling is also desirable from the viewpoint of the efficiency of the thermal power cycle. The cooling channels should be aligned along the dominant magnetic field (i.e., the poloidal field) to reduce coolant pressure and pumping power. For the particular configuration and the magnetic field strengths used in this study, heat flux of up to 3 MW/m^2 can be handled by both Li and Na with laminar flow and up to about 9 MW/m^2 with turbulent flow. In the case of turbulent flow, the tube wall must be electrically insulated to avoid excessive coolant pressure and pumping power. In an actual design, a proper combination of laminar and turbulent flow, and of complete turns and fractional turn of the coolant tubes will have to be used.

6.5.2. Water Cooling

The ability to cool the TITAN divertor is one of the key factors in the successful operation of the device. The peak flux encountered in the divertor may be in excess of 10 MW/m^2 (see Sec. 6.3). The best coolant for such high heat flux environments appears to be water in the forced convective sub-cooled boiling regime. The heat flux is normally from only one side. The heat flux and fluid flow conditions for a horizontal water-cooled copper alloy tube have recently been simulated with an electron beam heating apparatus [23]. Flow velocities up to 10 m/s and peak heat fluxes up to 10 MW/m^2 were used to cover the conditions expected for high heat flux components. Inlet water temperatures

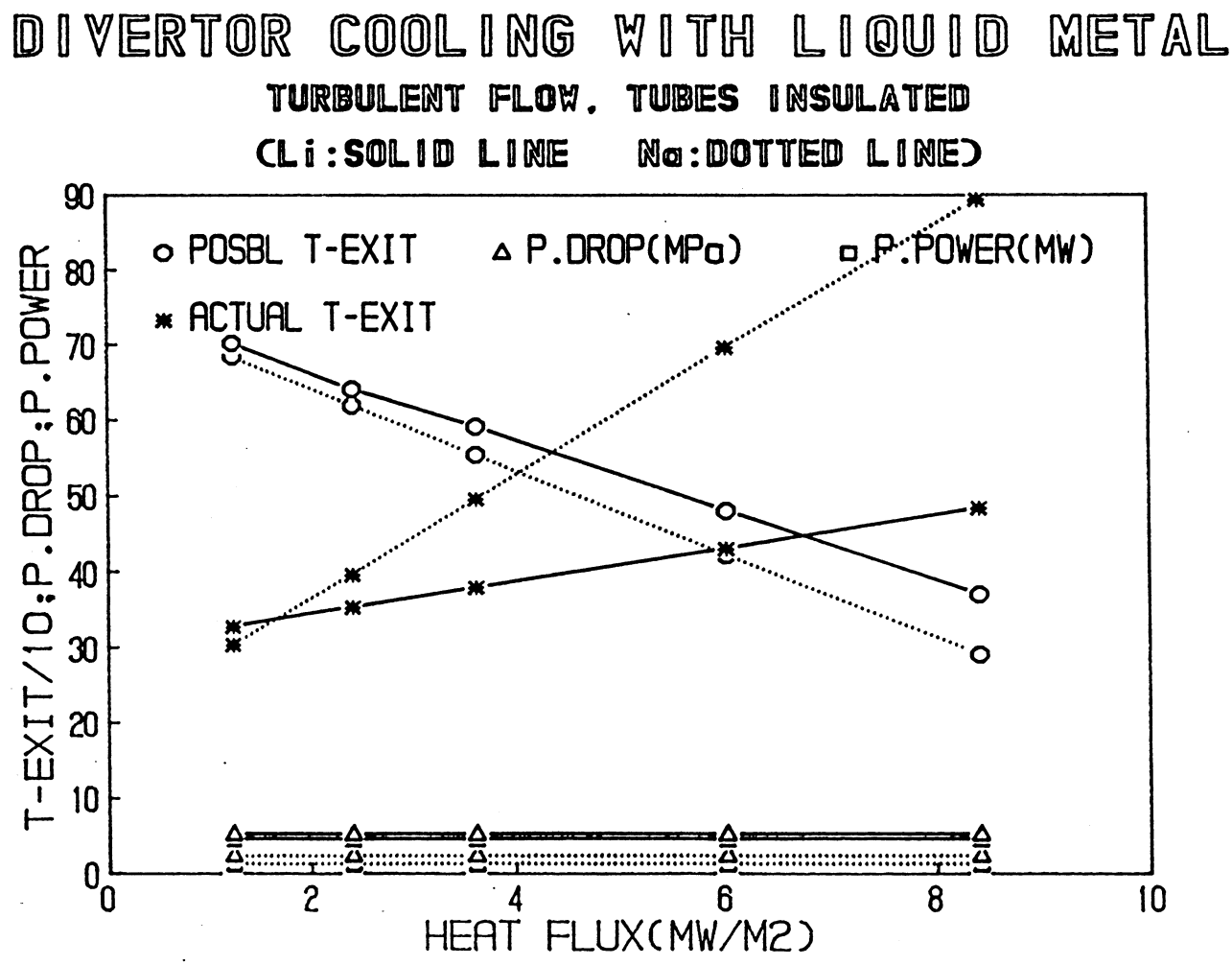

Fig. 6.5.-4. Variation of coolant exit temperature, pressure drop and pumping power with f_{RAD} or surface heat flux. The flow is turbulent and the tubes are electrically insulated.

of 30 °C and pressures of 17 atm were used throughout the test. The heated section of the tube was 8 cm long, leading to typical total temperature rises in the water of less than 15 °C. The tube inner diameter was about 1 cm, leading to a length to diameter ratio, L/D, of ~ 10. The resulting sub-cooled level was about 150 °C. According to the results of this experiment the tube can handle 18 MW/m^2 heat flux at a coolant velocity of 12 m/s without reaching the critical heat flux (CHF) limits. Based on these results it could be concluded that the existing correlations for uniformly heated tubes could be used as a guide to predict the CHF of a tube heated only on one side when the peak heat flux is used as the correlation parameter.

The length to diameter ratio, L/D, for the TITAN divertor plate is about 50 (L ~ 50 cm and D ~ 1 cm, assuming that the coolant flows normal to the poloidal field, i.e., in the "short" direction along the divertor plate as shown in Fig. 6.4.-2) which translates into a range for the CHF of 10 - 20 MW/m^2 for coolant velocities of 10 - 20 m/s. For higher heat removal rates than these values, therefore, an alternative approach should be investigated.

It is known that swirl flow in tubes can enhance the single phase heat transfer coefficient and increase the CHF in sub-cooled boiling by a factor of ~ 2 over the corresponding straight flow values for conditions under which the tubes are uniformly heated in circumference and length [24]. The correlation for CHF derived by Gambill et al [24] from experimental results shows that the CHF is about 1.5 times higher than the corresponding CHF for straight flow for various L/D. For example, the CHF at L/D = 50 for v = 10 m/s is about 17 MW/m^2 for swirl flow compared with 11.5 MW/m^2 for straight flow.

Milora et al [25] report that application of this correlation to a tube heated only on one side results in an underestimation of the critical heat flux. The improvement in CHF evidently results from the circulating flow pattern. The large component of tangential velocity in swirl flow apparently creates a situation in which sub-cooled fluid is continuously swept past the heated side of the tube. In the high heat flux target experiment at Oak Ridge [26], water cooled copper swirl tubes were used for the heat transfer medium. Tube burn-out did not occur even at normal heat fluxes greater than 50 MW/m^2. Although additional experiments are required to obtain CHF values for swirl flow existing evidence indicates that CHF may not be a limiting factor for the heat flux range envisaged for the TITAN divertor. The other limiting factors are discussed below. It is suggested, therefore, that swirl flow be utilized for the divertor cooling.

For the water-cooled blanket design the proposed coolant inlet temperature is about 290 °C with an exit temperature of 320 °C. A possible inlet coolant temperature for the divertor could be the same as the first wall/blanket inlet temperature. The exit coolant temperature from the divertor depends on the heated length of the tube and the heat flux on the tube surface. The exit coolant from the divertor could be mixed with the exit coolant from the first wall/blanket before entering the heat exchanger. In this flow configuration the thermal energy from the divertor could be converted to electricity with the same thermal cycle efficiency as for the water-cooled first wall/blanket. If for reasons which are discussed below the divertor coolant inlet temperature cannot reach 290 °C, the thermal energy of the divertor could be used for feedwater heating. However, the safety aspects of this flow configuration should be investigated since part of the primary loop will then be located outside the containment building.

It was mentioned earlier that CHF may not be a limiting factor for the heat flux range anticipated for the TITAN divertor. One important factor is the maximum temperature that the tube wall material can withstand. Copper alloy was selected as a candidate material because of its high thermal conductivity. Data for the effects of radiation damage are extremely limited, but it is known that the transmutation of copper to nickel and zinc reduces the thermal conductivity. A value of 110 W/mK was used in this study, representing an end of life value and a factor of ~ 3 lower than for the unirradiated material. It is assumed that the maximum wall temperature limit applies to the mid-section of the tube wall (rather than the outside), and the maximum allowable temperature is taken as 450 °C (see Sec. 8.3.4). Based on these assumptions the maximum inner wall temperature of the copper alloy should not exceed 405 °C for a 1 mm wall thickness and a heat load of 10 MW/m^2. This temperature drops to 360 °C for the 20 MW/m^2 case.

The maximum heat removal capability of a coolant occurs in the fully developed sub-cooled boiling regime, where the main driving force is the difference between the wall temperature and the coolant saturation temperature (ΔT_{SAT}). The wall and coolant temperature distributions in a sub-cooled boiling regime are shown in Fig. 6.5.-5 [27]. In the divertor plate configuration where the plate is heated only on one side, the heat transfer at the wall-coolant interface is dominated by forced convective sub-cooled boiling on the heated side and by liquid single phase forced convection on the unheated side. Correlations for swirl flow heat transfer coefficients under these conditions

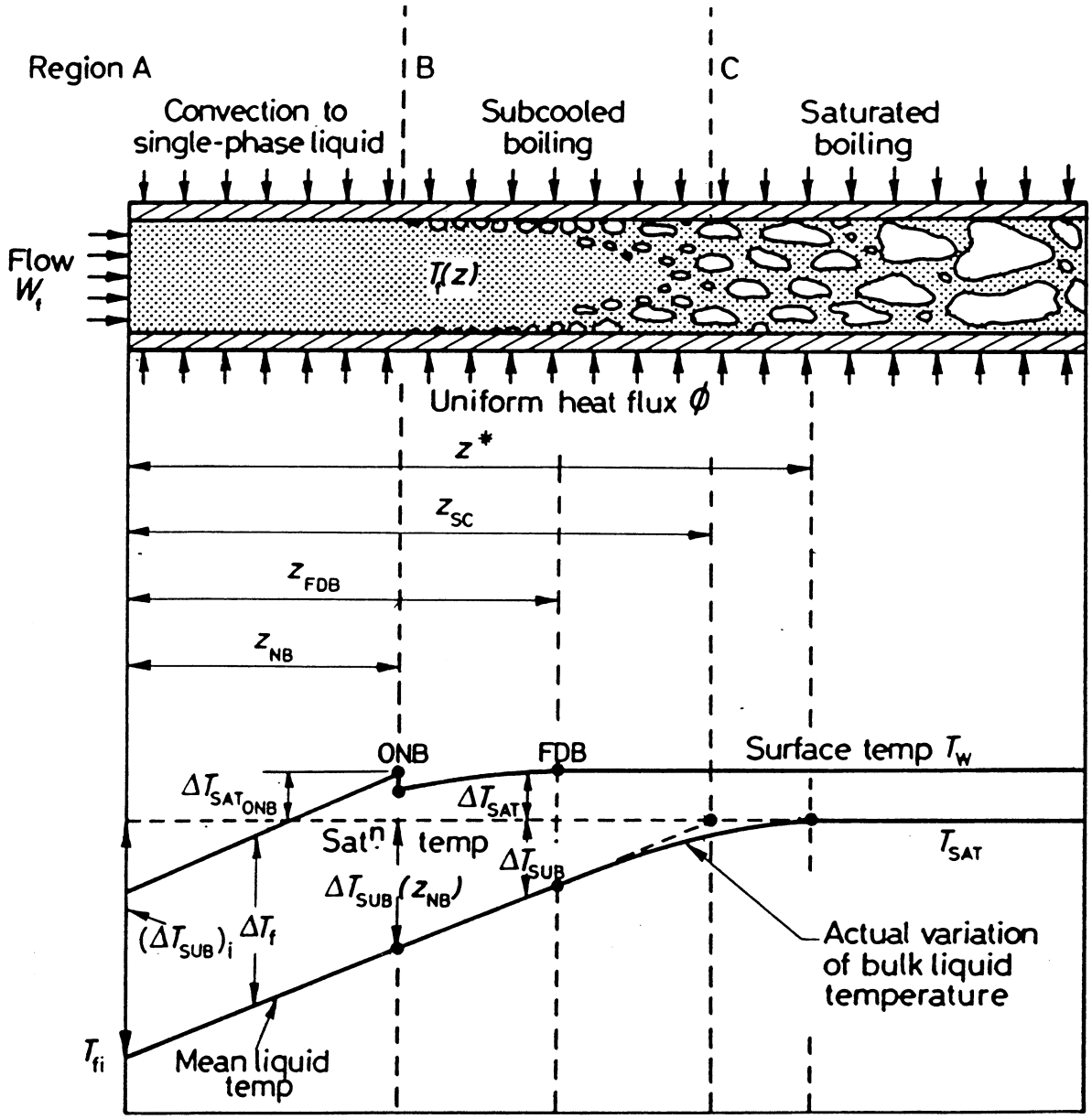

Fig. 6.5.-5. Surface and liquid temperature distributions in sub-cooled boiling [27].

are not available. The correlation developed by Thom et al [28] for uniformly heated tubes in the forced convection sub-cooled boiling regime was chosen here to predict the ΔT_{SAT} at the point of peak heat flux. This method may be conservative since the lateral heat conduction in the tube wall reduces the heat flux to the coolant at the point of peak heat flux.

Table 6.5.-I shows the coolant conditions through a copper-alloy tube with L/D = 60 for heat fluxes in the range from 5 to 20 MW/m². The coolant is water with an inlet temperature and pressure of 290 °C and 150 atm respectively. The coolant velocity is taken to be 10 m/s. The second column of this table shows the upper temperature limit at the inner tube wall for a tube wall thickness of 1 mm. The next two columns give the temperature at this location at the tube inlet and outlet assuming that forced convection is the only mechanism of heat transfer operating . For these coolant conditions the wall temperature required for the onset of subcooled boiling, T_{ONB}, is 346 °C. As this temperature is higher than the outlet wall temperature for purely forced convection at a heat flux of 5 MW/m² no boiling will occur for this case.

TABLE 6.5.-I

Water coolant flow conditions for various heat fluxes

(L/D = 60, v = 10 m/s, T_{in} = 290 °C, p = 150 atm)

q (MW/m²)	T_{imax} (°C)[2)]	T_{iw} (°C)[1)] inlet	T_{iw} (°C)[1)] outlet	T_{FDB} (°C)
5	412	326	336	352
10	405	362	381	356
15	382	398	425	359
20	360	434	470	361

1) T_{imax} is the maximum allowable temperature at the inside of the tube wall and is based on a maximum allowable temperature of 450 °C for copper alloy at the mid-section of the tube wall and on a wall thickness of 1 mm.

2) T_{iw} is the inner tube wall temperature assuming that forced convection is the only heat transfer mechanism.

At heat fluxes of 10 MW/m^2 and higher the predominant heat transfer mechanism is sub-cooled boiling as the wall temperature is higher than the fluid saturation temperature. The wall temperature at which fully developed sub-cooled boiling starts, T_{FDB}, is shown in the last column of Table 6.5.-I. At a heat load of 20 MW/m^2, T_{FDB} = 361 °C which is only 1 degree above the upper temperature limit at the inner wall. This means that it is possible to transfer about 20 MW/m^2 of heat to the high temperature coolant by the forced convection sub-cooled boiling mechanism through a copper-alloy coolant tube.

6.5.3. Helium Cooling

6.5.3.1. Introduction

Helium can be a suitable coolant for high heat flux components but usually requires high temperature operation. Helium has a high heat capacity, is chemically inert and is transparent to neutrons. The gas itself does not impose any limitations on the operating temperature range of a system; the maximum coolant temperature is dictated by the structural material temperature limit. If high temperature materials are used, helium as a coolant can sustain high thermal power conversion efficiencies. But due to its low specific weight the use of helium is restricted by a limited gas-side heat transfer coefficient, high operating pressure and relatively high pumping power. These limitations do not always appear in isolated assessments of the gas-side heat transfer capabilities. The parametric study reported here aims at evaluating the maximum heat fluxes that can be removed from a realistically designed cooled surface exposed to a uniform, planar heat source. The focus is on the thermal-hydraulic aspects of the task.

6.5.3.2. Materials

Symbol	Units	Definition
α	K^{-1}	Mean thermal expansion coefficient
E	GPa	Modulus of elasticity (Young's modulus)
k	W/mK	Thermal conductivity
ν		Poisson's ratio
S_{mt}	MPa	Design stress limit
T	K	Temperature
T_{wmax}	K	Maximum wall temperature limit

The following materials and property data are considered:

Copper alloy (Cu). This material has an excellent thermal stress parameter and fabrication and manufacturing capabilities are well established. Although Cu is commercially available the data base for the irradiated material is sparse. The following property correlations, with estimated irradiation effects included for S_{mt}, are used in the calculations.

α	=	$3.257 \times 10^{-6} + 37.5 \times 10^{-9}$ T	K^{-1}	*)
E	=	143.68 - 0.105 T	GPa	*)
k	=	110	W/mK	
ν	=	0.34		
S_{mt}	=	100	MPa	
T_{wmax}	=	723	K	

*) based on AMAX-MZC [1]

SiC/SiC composite. SiC is a ceramic with very high temperature capability. The irradiation resistance and activation is presumably relatively good. Manufacturing (woven fiber in a chemical vapor deposited matrix) is in the early stages of development. The following property correlations [29] are used here; irradiation effects and maximum wall temperature limits are estimated.

α	=	4.9×10^{-6}		K^{-1}
E	=	440		GPa
k	=	15		W/mK
ν	=	0.24		
S_{mt}	=	350	tensile	MPa
		700	compressive	MPa
T_{wmax}	=	1473		K

Vanadium alloy (V). Vanadium is a high temperature, high strength material, developed mainly in LMFBR programs, and has good radiation resistance in alloys such as V-3Si-1Ti. The following property correlations are used here based on V-15Cr-5Ti [10]:

α	=	$8.95 \times 10^{-6} + 1.75 \times 10^{-9}$ T	K^{-1}	
E	=	132 - 0.018 T	Pa	
k	=	17.6 + 0.0135 T	W/mK	
ν	=	0.36		
S_{mt}	=	105	MPa	for T < 975 K
		300 - 0.26 T	MPa	for T > 975 K
T_{wmax}	=	973	K	

6.5.3.3. Analysis

The configuration for the analysis is given in Fig. 6.5.-6. Straight tubes of a given inside diameter, d_i, outside diameter, d_o, and length, L, are arranged in a bank which is exposed to a unilateral and uniform heat flux, $\dot{q}$. These tubes are made of one of the materials referred to in Sec. 6.5.3.2. Helium at temperature T_{He1} enters the tubes at static pressure p_{He1} and leaves them at temperature T_{He2} and pressure p_{He2}. Complete mixing of the gas is assumed. The pressure drop calculation is based on a standard procedure with a recursive formula for the determination of the friction factor, to be multiplied with the mean pressure head [30].

The critical location for the heat transfer is at the tube exit where the maximum wall temperature limit, T_{wmax}, may not be exceeded. A one-dimensional radial heat transfer analysis is performed in the direction of the heat flux. This analysis consists of a conductive and a convective part. Depending on the material type two different procedures are followed to determine the linear temperature profile through the wall: for metals the limiting T_{wmax} is applied to the midsurface of the wall, whereas for ceramic materials T_{wmax} is applied to the outer surface. In both cases the material properties are evaluated for the respective temperature in the wall midplane. The convective gas-side heat transfer is based on a formula by DalleDonne [30]

$$Nu = 0.022\ Re^{0.8}\ Pr^{0.4} \left[\frac{T_{if2}}{T_{He1}}\right]^{-0.18} \qquad (6.5.-1)$$

where T_{if2} is the gas-side wall interface temperature at the tube outlet.

No corrections for either non-uniform heat flux or short tubes are made. For enhanced heat transfer 2-D surface roughening is assumed to increase the

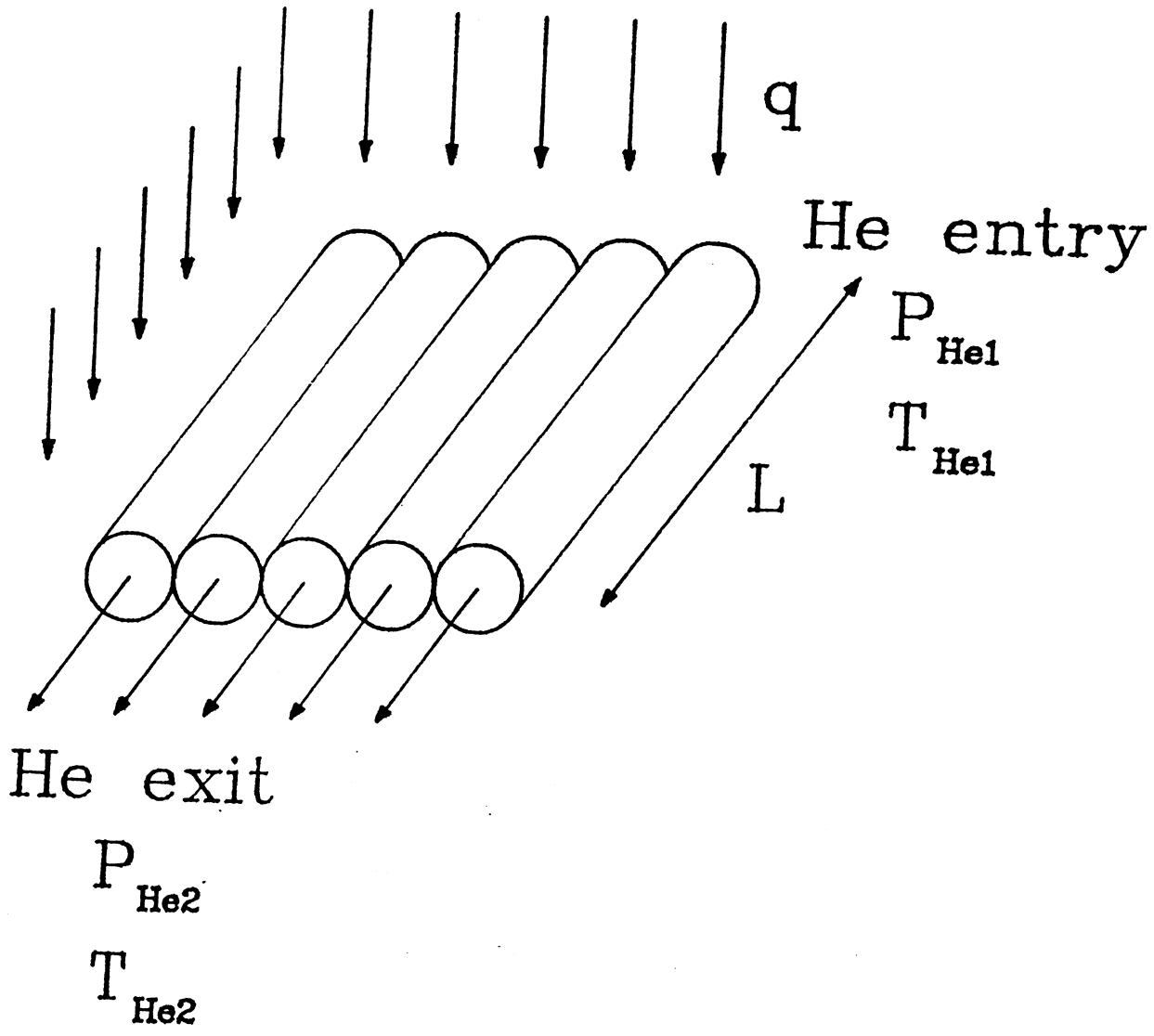

Fig. 6.5.-6. Configuration for helium cooling: planar tube bank with uniform heat flux.

above-mentioned heat transfer coefficient by a factor of 2.4 while multiplying the friction factor by 4.

A thin wall tube stress estimation is also made. For the thermal stress a cosine outside temperature profile around the tube and a constant inside temperature are assumed. The tubes are treated as radially free while axially completely restrained. In the following formulae, which are exact for these conditions, σ_1 is the hoop stress and σ_{2rad}, σ_{2axc} and σ_{2axt} are the circumferential, axial compressive and axial tensile components of the thermal stress [31].

$$\sigma_1 = \frac{p_{He1}\ d_i}{(d_o - d_i)} \qquad (6.5.-2)$$

$$\sigma_{th} = \alpha\ E\ \Delta T_{wall} \qquad (6.5.-3)$$

$$\sigma_{2rad} = \pm \frac{\sigma_{th}}{2\ (1 - \nu)} \qquad (6.5.-4)$$

$$\sigma_{2axc} = -\ 0.75\ \sigma_{th} \qquad (6.5.-5)$$

$$\sigma_{2axt} = +\ 0.25\ \sigma_{th} \qquad (6.5.-6)$$

These components of the two-dimensional stress are combined in an equivalent von Mises stress, σ_{vM}, tensile for the inner, compressive for the outer surface, neither to exceed the 3 S_{mt} limit for secondary stresses.

6.5.3.4. Results

With respect to the high heat flux heat removal requirements of TITAN, particularly for the cooling of divertors, the analysis described here is used to determine the limitations of helium cooling. Based on a probable TITAN environment the following set of input parameters is chosen for a base-case comparison among the three materials selected in Sec. 6.5.3.2:

d_i = 10 mm	d_o = 12 mm
L = 0.75 m	p_{He1} = 10 MPa
smooth surface	T_{wmax} as stated in Sec. 6.5.3.2

The mass flow rate through the tubes and the helium inlet temperature are varied such that the maximum wall temperature limit, T_{wmax}, at the tube exit cross section is exactly matched and at the same time none of the following limiting criteria is violated.

$$M_2 < 0.3 \qquad r_p < 0.1 \qquad f_P < 0.1$$

where M_2 is the Mach number at the tube outlet, r_p is the pressure ratio (pressure drop divided by the system pressure) and f_P is the pumping power fraction (based on the thermal power removed).

For the set of parameters chosen it is the pumping power fraction criterion which dominates; therefore all results presented here show the maximum achievable temperature level with $f_P = 0.1$. Among the stress limitations, $\sigma_1 < S_{mt}$ and $\sigma_{vM} < 3\ S_{mt}$, the combined stress criterion is effective only in a few cases with heat fluxes in the 10 MW/m² range (see Fig 6.5.-10).

Some results of the base case calculations for the three selected materials are presented in Fig 6.5.-7. Due to its relatively low maximum wall temperature limit Cu cannot handle more than 8 MW/m², based on an inlet temperature limit set close to the environmental temperature of about 300 K. A coolant outlet temperature at which the heat removed is capable of generating electricity in a HTGR cycle would require $T_{He2} > 475$ K (based on extrapolated data from reference [32]). Applying this more restrictive criterion the maximum nominal heat flux for Cu is less than 5 MW/m². Both SiC and V can handle 8 - 10 MW/m² depending on the criteria. For nominal heat fluxes up to 7 MW/m² SiC has a considerable temperature advantage over V. This lead, however, quickly disappears for higher heat loads due to the more restrictive approach in the use of T_{wmax} and the somewhat lower thermal conductivity.

Fig 6.5.-8 shows the corresponding figures for SiC only. In addition to the base case data, the results for roughening the surface, doubling the wall thickness or doubling the tube length are given. Due to the aforementioned differences in the conductivity evaluation, SiC is particularly sensitive to an increase of the wall thickness. (It should be noted that the base case wall thickness of 1 mm, which probably represents a lower feasibility limit for a ceramic composite, is also applied for SiC here.) Due to its superior thermal conductivity, Cu is the least affected by thicker walls.

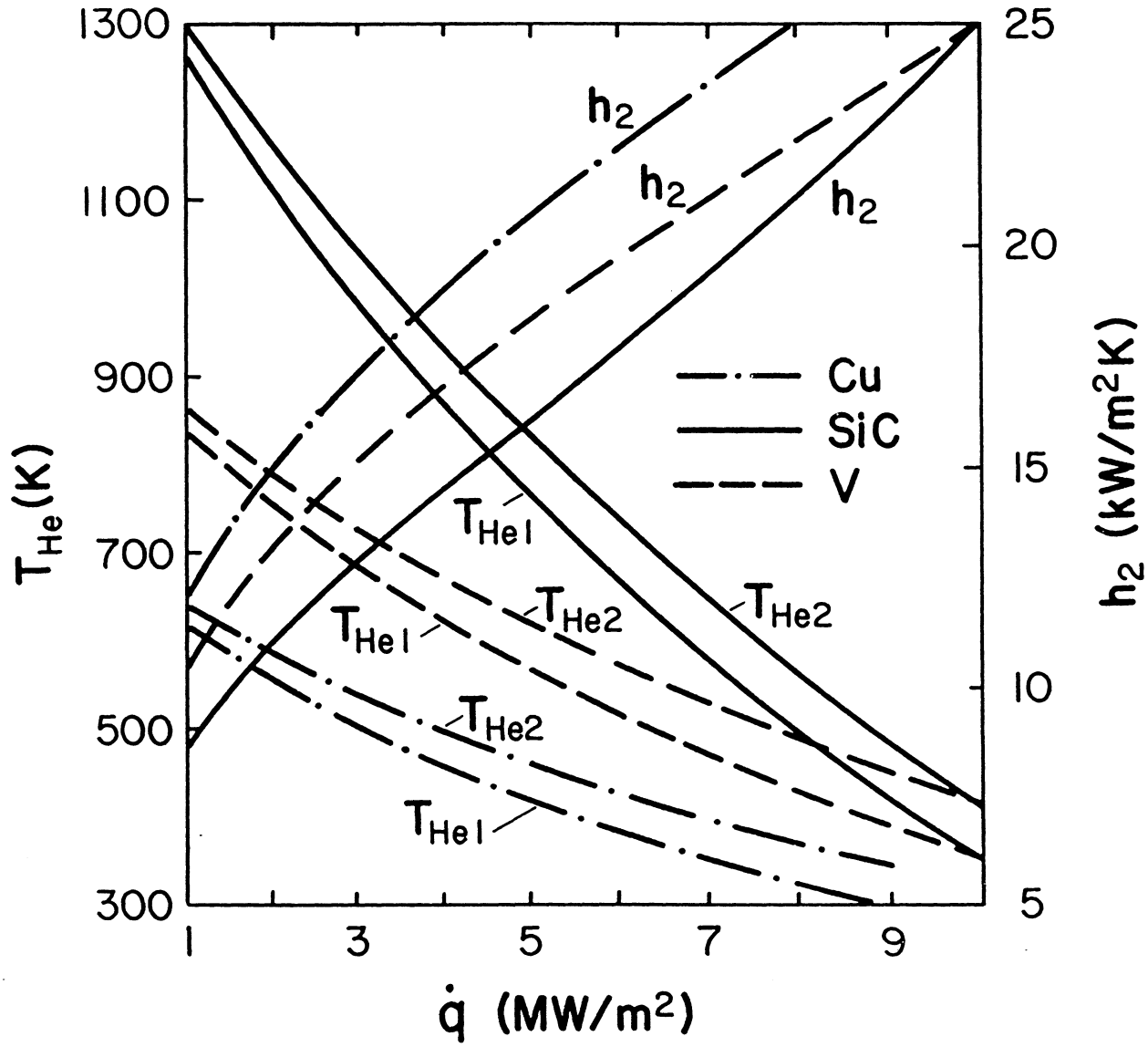

Fig. 6.5.-7. Results of base case calculations for the three materials indicated. (Base case: d_i = 10 mm, d_o = 12 mm, L = 0.75 m, p_{He1} = 10 MPa, smooth surface)

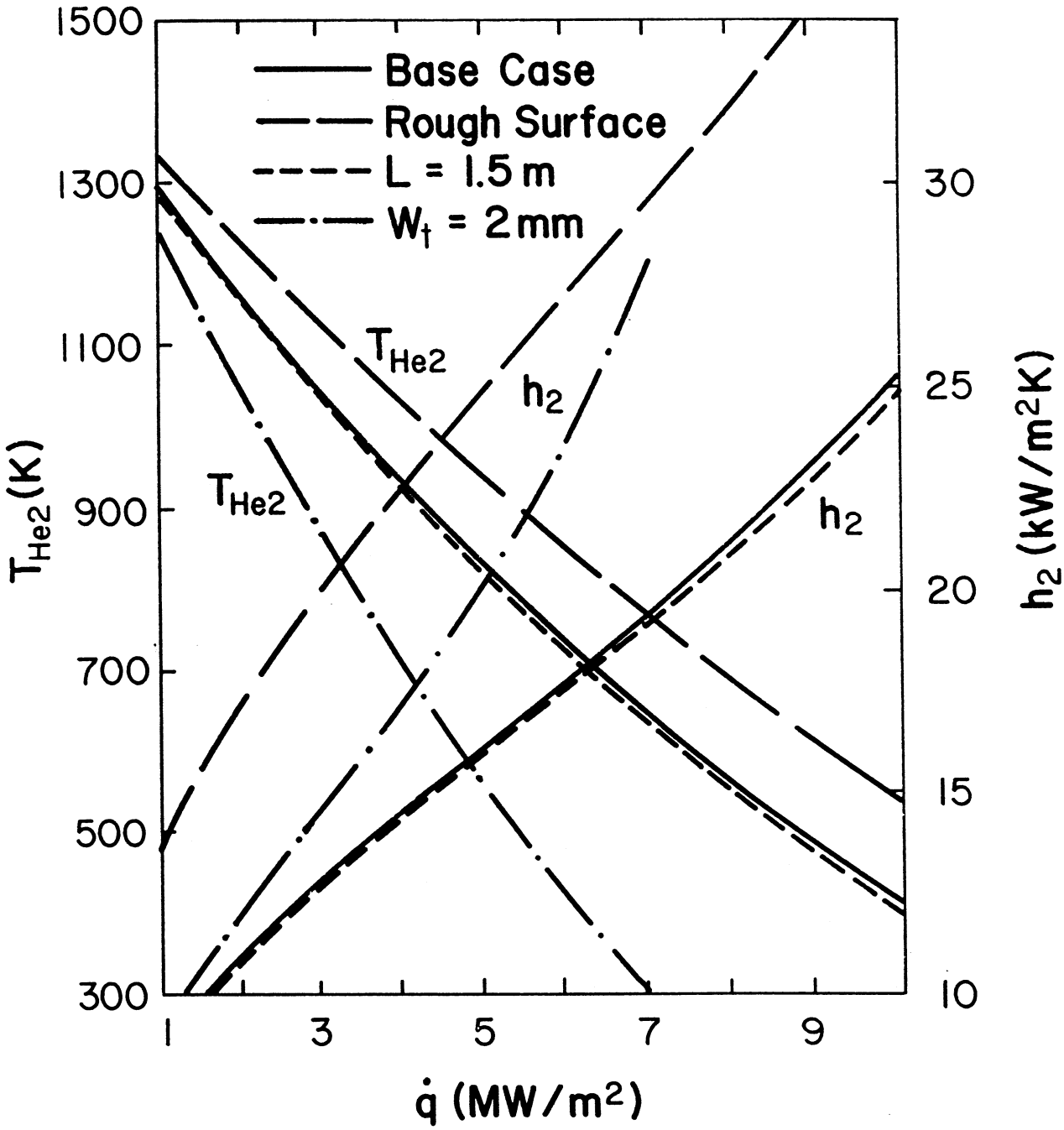

Fig. 6.5.-8. Comparison of SiC base case results with calculations for roughening the tube surface, doubling the tube length to L = 1.5 m or doubling the tube wall thickness to d_i = 10 mm and d_o = 14 mm. (Base case: d_i = 10 mm, d_o = 12 mm, L = 0.75 m, p_{He1} = 10 MPa, smooth surface)

The suitability of the different materials for different wall thicknesses and nominal heat fluxes can be assessed without considering the gas-side heat transfer. The gas-side wall interface temperature, T_{if}, as a function of wall thickness and heat flux is governed by the maximum wall temperature limit and the conductivity of any given material. Fig 6.5.-9 shows the lines of equal T_{if} for the three material combinations. Along a line of equal T_{if} the two respective materials produce identical gas-side heat transfer conditions and are therefore equivalent from a thermal-hydraulic point of view. The material with higher thermal conductivity, but lower maximum wall temperature limit becomes preferable when moving away from this line in the direction of higher $\dot{q}$, higher wall thickness, W_t, (as indicated in Fig. 6.5.-9), and vice versa. Fig. 6.5.-10 presents the thermal stress limits and the combined stress limits at 10 MPa pressure difference across the tube wall. As the primary stress affects this limit only marginally, combining Fig. 6.5.-9 and Fig. 6.5.-10 results in a chart (Fig. 6.5.-11) which shows the thermal-hydraulically preferred material for a given combination of wall thickness and heat flux while at the same time satisfying the stress criterion.

6.5.3.5. Conclusion

This study shows that helium cooling is capable of handling nominal heat fluxes of up to 10 MW/m^2. Vanadium and SiC would permit high temperature operation. Vanadium is the material of choice for tubes with wall thickness between 0.5 and 1.0 mm, thicknesses that are thin for a ceramic composite.

To increase the reliability of the results presented the material data base needs a substantial expansion for the properties of irradiated materials. The evaluation of stresses could be improved with a 2-D analysis of the conductive heat transfer in the exit cross section of the tubes. Finally the asymmetric heat flux in the tubes enhances the build-up of hot streaks which are not accounted for in this study.

6.5.4. Innovative Concepts

Modeling of the divertor plasma suggests that the peak heat flux at the divertor target will be high. Some effort has therefore been spent in examining innovative concepts which may have the potential to accommodate higher heat loads and at the same time are resistant to damage by sputtering.

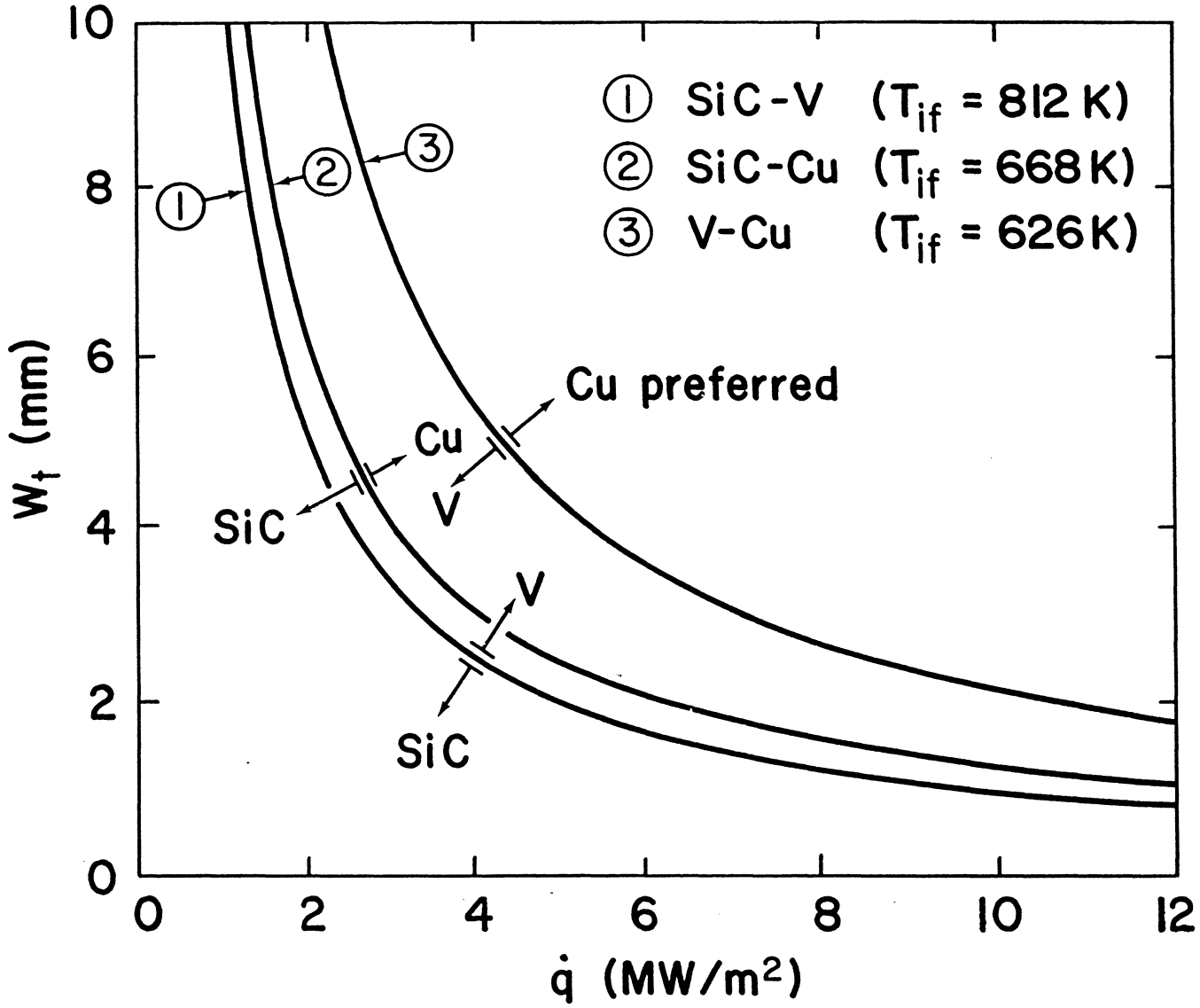

Fig. 6.5.-9. Equal interface temperature, T_{if}, lines

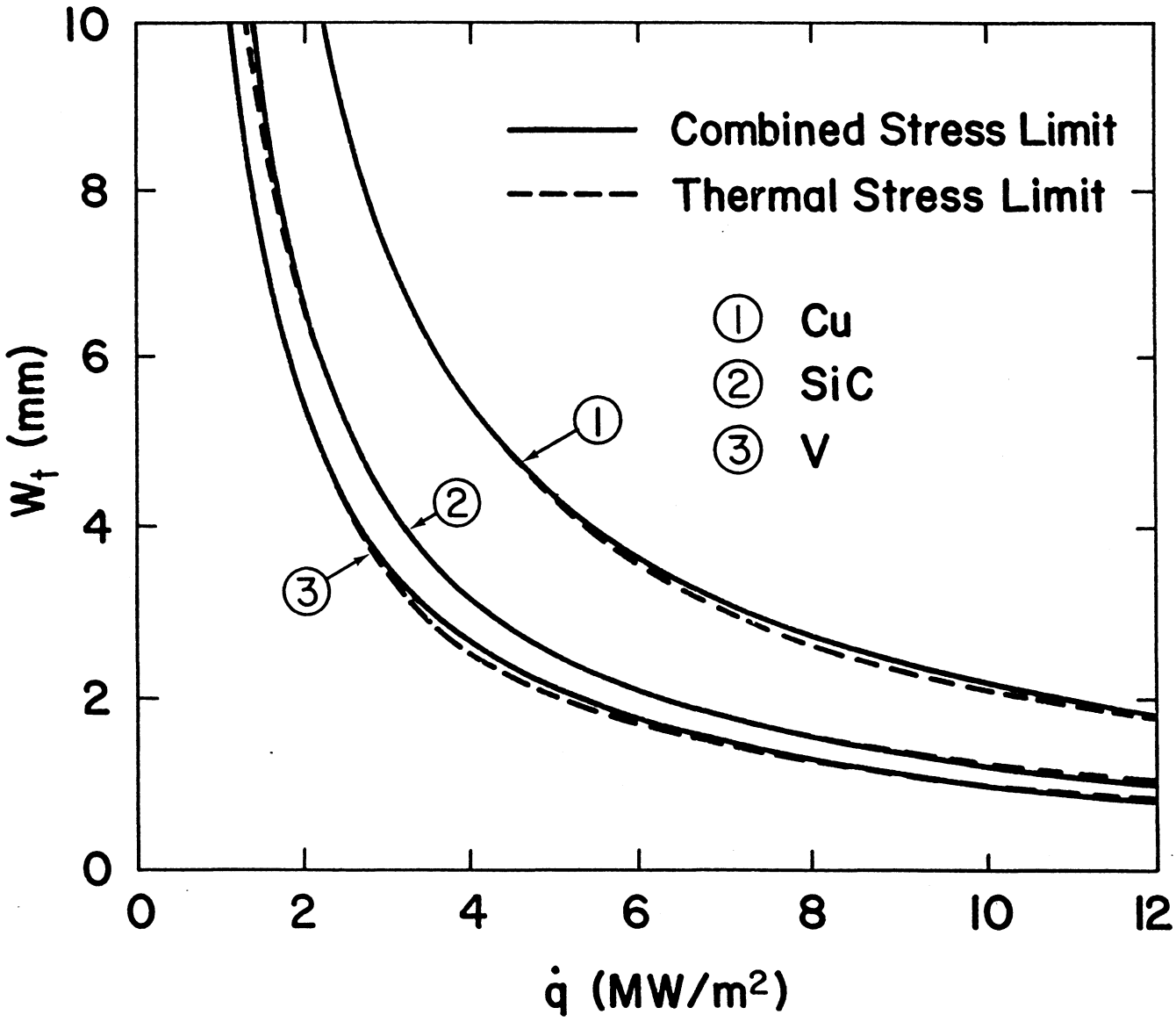

Fig. 6.5.-10. Thermal stress limit and combined (primary and secondary) stress limit at 10 MPa gas pressure difference across the tube wall.

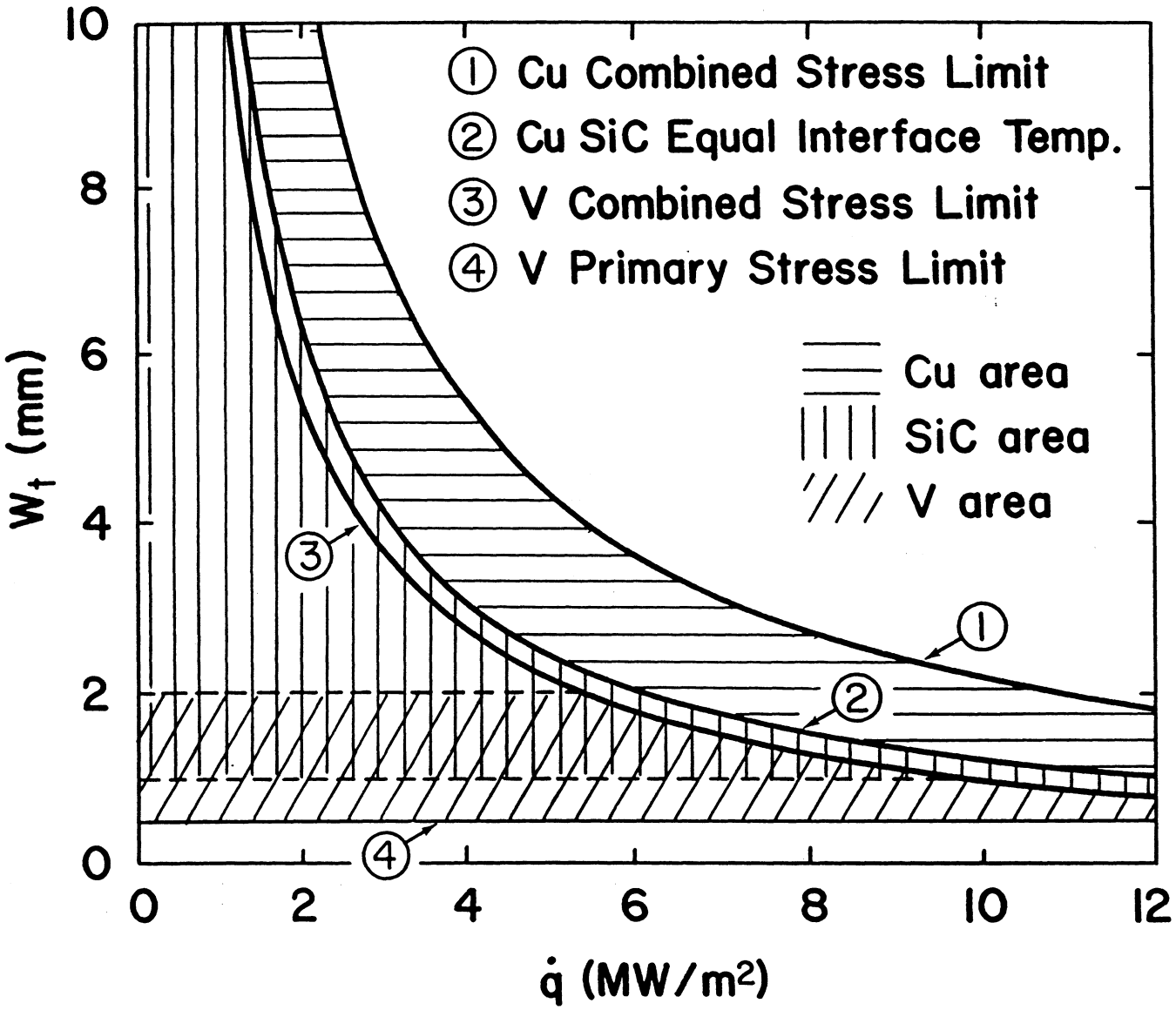

Fig. 6.5.-11. Preferred material selection for a given combination of nominal heat flux and wall thickness; combined stress limit satisfied for 10 MPa pressure difference across the tube wall.

One approach involves allowing the divertor plasma to strike a liquid metal surface. The liquid will heat up, vaporize and condense on a cooler surface, such as the divertor chamber wall. As the condensing material will carry heat the load will have been spread over a larger area. The liquid metal could be supplied by seepage through a porous wall material such as for the INPORT design in the HIBALL inertial fusion reactor design [33].

To assess the feasibility of the concept a simple energy balance calculation was carried out. Assuming that all the power transported to the divertor is used to heat the liquid from its melting point to its boiling point and then to vaporize it, the mass flow rate required for various liquids was evaluated. For a value of f_{RAD} of 0.5 (corresponding to ~ 250 MW of power transported to the divertor) the mass flow rate varies from 10 kg/s for lithium to ~ 100 kg/s for liquid tin. From the mass flow rate an estimate was made of the neutral pressure of the evaporating material in the divertor chamber. Because the volume of the pressure chamber is relatively small the steady state neutral pressure is high, > 0.1 atm. Such a high pressure would cause a very large backflow of neutrals to the core plasma and the resultant contamination would be excessive.

An alternative approach which has been briefly examined involves the formation of a cloud of lithium droplets to intercept the divertor plasma stream. This concept was described in detail in references [34-36]. A cloud of fast moving lithium droplets is formed by an array of nozzles fed by high pressure liquid in a region of low magnetic field strength. The charged particles in the divertor plasma strike the droplets, are captured (lithium acts as a strong getter for hydrogen) and deposit their energy. To prevent significant evaporation of the droplet occurring (leading to the problem of high neutral pressure encountered above) the velocity of the droplet must be high, so that it spends only a short time subjected to the high heat flux. Although the divertor plasma forms a poloidally continuous ring it may only be possible to intercept it at one poloidal location (or over a limited range of poloidal angle), on the outboard side of the torus, to avoid the danger of the droplet cloud entering the main plasma. The reduced area for collecting the plasma increases the heat load correspondingly. Two possible configurations are shown in Fig. 6.5.-12.

A simple calculation has been performed to estimate the velocity of the droplet in order that the overall temperature rise (assumed uniform through the pellet) is limited to 500 °C. For the first option in Fig. 6.5.-12 a velocity

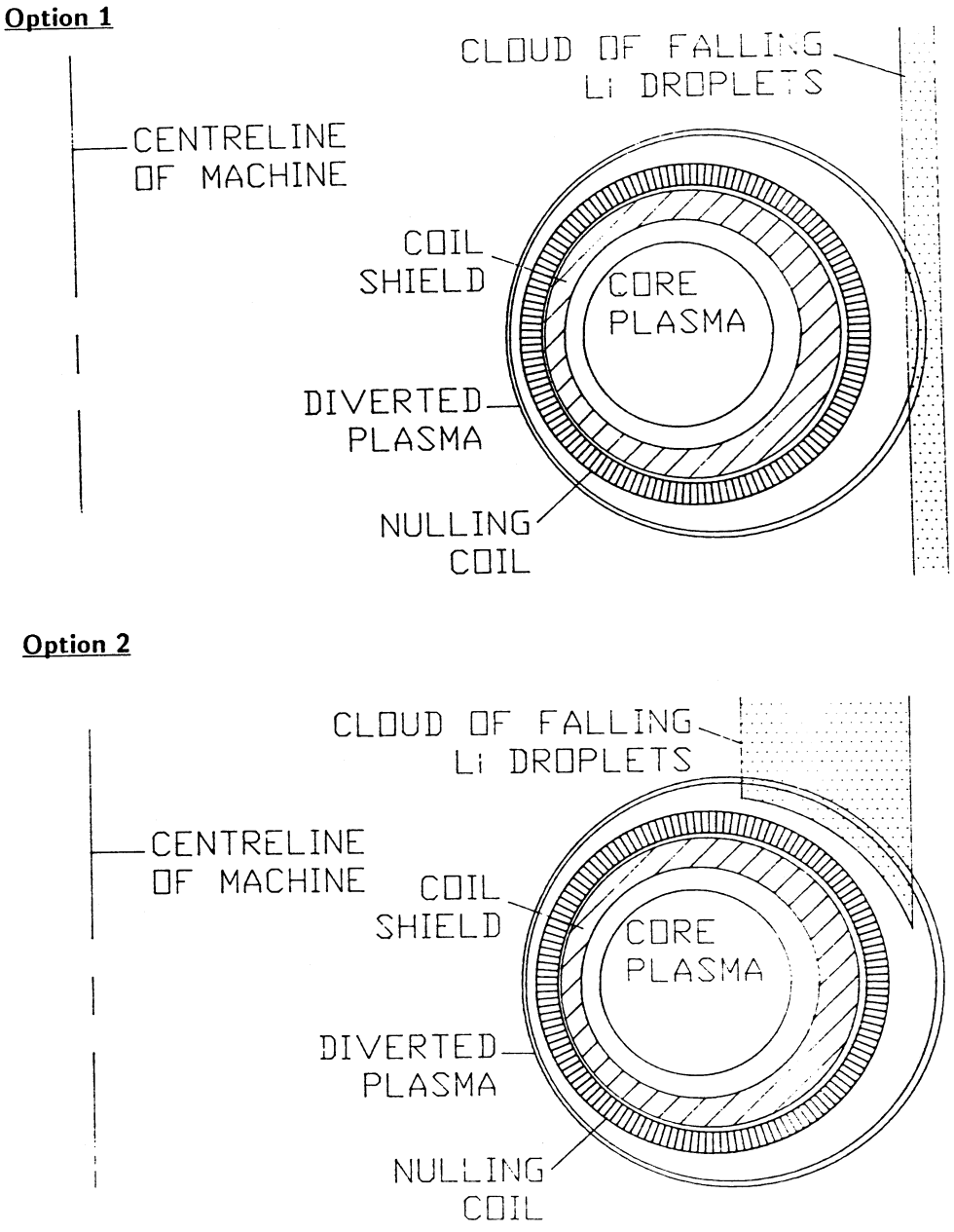

Fig. 6.5.-12. Schematic diagram showing two options for the configuration of the lithium droplet cloud.

of ~ 1 km/s is required, which is far too high for a feasible design. The velocity necessary for option 2 is ~ 50 m/s, implying that a pressure of ~ 1 MPa at the nozzle is required. Further investigation of the approach will need to include the temperature distribution through the droplet [37] to ensure that hot spots do not cause localized vaporization. A major design issue will be for a mechanism to collect the lithium droplets after they have passed through the plasma.

6.6. CONCLUSIONS AND FUTURE WORK

A poloidally-symmetric toroidal field divertor is to be used for the impurity control system in TITAN. This choice is based on the problems of erosion and plasma contamination associated with limiters and on the original work on divertors for reversed field pinches in the CRFPR design [5,7].

Magnet configurations for the divertor have been produced using a two-dimensional analysis. The closed geometry which is obtained (unlike the open geometry which is generally employed in poloidal divertors for tokamak reactors), due to the proximity of the divertor coils to the plasma, allows the divertor chamber to be decoupled from the plasma chamber and leakage or backflow of neutral particles from the divertor to the main plasma should be minimal. This closed configuration also tends to cause the flux surfaces in the divertor to be compressed, increasing the heat load on the divertor plate. The use of additional coils in order to expand the flux in this region was investigated but found not to be cost-effective. Examination of an open divertor is warranted on the basis of its apparent lack of poloidal asymmetries and flux expansion.

The Integrated-Blanket-Coil (IBC) approach has been considered for the divertor with the liquid metal cooled blanket design and provides several advantages over a design with conventional copper coils. The loss of breeding blanket coverage due to the multiple divertors (~ 10 % for the CRFPR [5]) is greatly reduced and the coils can be located closer to the plasma (offsetting the higher Ohmic losses in the IBC coils).

Modeling of the edge-plasma, using both analytic models and one-dimensional radial transport codes, indicates that the characteristic thickness for the radial decay of power flow in the scrape-off layer will be small, ~ 1 cm, implying high power loads on the divertor target. Injection of high Z impurities into the divertor plasma to radiate the incident power over a wider area has been examined and impurity fractions on the order of a few per cent are

necessary to reduce the heat flux to the divertor target significantly. An increase in the core plasma radiation fraction to > 0.75 is also suggested to reduce heat loads further. The possibility of using impurity radiation in the scrape-off layer to reduce the divertor heat load and to reduce the plasma temperature at the first wall and divertor target (hence, reducing the sputtering rate) appears attractive and will be investigated in the future.

Several cooling options for the divertor have been examined. Liquid metal cooling in the turbulent regime with electrically insulated tube walls (to minimize the MHD pressure drop and pumping power) allows heat loads of up to 9 MW/m^2 to be accommodated. Water-cooled copper tubes using swirl flow permit about 20 MW/m^2 of heat flux in the forced convection sub-cooled boiling heat transfer regime. With helium cooling up to 10 MW/m^2 is achievable although at this heat flux the heat is not removed at temperatures of interest for power generation. A brief investigation of innovative concepts has been made. Spreading the heat load by vaporization and remote condensation of a liquid metal has been shown to be infeasible because of the high pressure of the vaporized material which results. The use of a cloud of lithium droplets to intercept the divertor plasma may be possible but the droplet must have a high velocity to minimize its temperature rise.

Future work on the divertor will concentrate on the IBC approach for the Li/V blanket design. For the water-cooled design a study will be made of life-limiting processes for highly irradiated copper coils to determine their shielding requirements. A three-dimensional analysis of the magnetic configuration is necessary to study magnetic islands introduced by the divertor coils and the inboard-to-outboard asymmetries of the field lines to ensure that an acceptable divertor design is obtained.

The feasibility of confining the injected impurities in the divertor plasma will be examined with edge-plasma models. Improved neutral particle models will be incorporated to simulate recycling in the divertor and to allow a more accurate estimate of the plasma conditions at the divertor target to be made. The core and edge-plasma models will be coupled to ensure self-consistency of heat and particle fluxes. Profiles of plasma parameters in the scrape-off layer will be used to calculate the erosion rate at the first wall.

As the design progresses more detailed calculations on the thermal hydraulics and stress analysis of the divertor cooling will be made. The vacuum pumping system will be analysed to ensure that a large enough pumping speed can be attained to accommodate the required gas throughput.

These efforts will allow a more complete and credible divertor design to be achieved which will be integrated with the rest of the fusion power core design.

REFERENCES

1. C. C. Baker et al., "STARFIRE - A Commercial Tokamak Fusion Power Plant Study", Argonne National Laboratory Report ANL/FPP-80-1 (September 1980).

2. INTOR Phase One, Report of the International Tokamak Reactor Workshops 1980-81, IAEA, Vienna (1982).

3. P.I.H. Cooke, P. Reynolds et al., "A DEMO Tokamak Reactor - Aspects of the Conceptual Design", Culham Laboratory Report CLM-R254 (August 1985).

4. R. L. Hagenson, R. A. Krakowski, C. G. Bathke, R. L. Miller et al., "Compact Reversed Field Pinch Reactors (CRFPR) - Preliminary Engineering Considerations", Los Alamos National Laboratory Report LA-10200-MS (August 1984).

5. C. Copenhaver, R. A. Krakowski, N. M. Schnurr, R. L. Miller, C. G. Bathke, R. L. Hagenson et al., "Compact Reversed Field Pinch Reactors (CRFPR) - Fusion Power Core Integration Study", Los Alamos National Laboratory Report LA-10500-MS (August 1985).

6. C. G. Bathke, R. L. Miller and R. A. Krakowski, "Magnetic Divertor Design for the Compact Reversed Field Pinch Reactor", Proceedings of the 13th Symposium on Fusion Technology, Varese, Italy, September 1984, 1259.

7. C. G. Bathke, R. A. Krakowski and R. L. Miller, "A Comparison of Toroidal-Field Divertors for a Compact Reversed Field Reactor", 6th Top. Mtg. on the Technology of Fusion Energy, San Francisco, CA, (March 1985).

8. P. Thullen, K. Schoenburg (eds.), "ZT-H RFP Experiment Technical Proposal", Los Alamos National Laboratory Report LA-UR-84-2602 (June 1984).

9. M. A. Mahdavi et al., "Particle Exhaust from Plasma Discharges with an Expanded Boundary Divertor", Phys. Rev. Lett. 47 (1981) 1602.

10. D. L. Smith, G. D. Morgan et al., "Blanket Comparison and Selection Study - Final Report", Argonne National Laboratory Report ANL/FPP-84-1 (September 1984).

11. P. J. Harbour, "Thickness of the Scrape-off Layer of a Large Tokamak with a Poloidal Divertor", Nucl. Fusion, 24 (1984) 1211.

12. A. K. Prinja and R. W. Conn, "An Axially Averaged Radial Transport Model of Tokamak Edge Plasmas", J. Nucl. Mater. 128 & 129 (1984) 135.

13. A. K. Prinja, R. F. Schaffer, R. W. Conn and H. C. Howe, "Combined Core/Boundary Layer Transport Simulations in Tokamaks", to be published in J. Nucl. Mater. (1986).

14. A. Bond, P. I. H. Cooke and E. S. Hotston, "A Liquid Metal Protected Divertor for a DEMO Reactor", Proceedings of the 13th Symposium on Fusion Technology, Varese, Italy, September 1984, 1225.

15. M. Shimada et al., "Heat Load Reduction of the Divertor Plate and Formation of Dense and Cold Plasma by Remote Radiative Cooling in Doublet III and INTOR", JAERI Report JAERI-M 9862 (December 1981).

16. D. E. Post, R. V. Jensen, C. B. Tarter, W. H. Grasberger and W. A. Lokke, "Steady State Radiative Cooling Rates for Low Density High Temperature Plasmas", At. Data and Nucl. Data Tables 20 (1977) 397.

17. J. Neuhauser, W. Schneider, R. Wunderlich and K. Lackner, "Modeling of Impurity Flow in the Tokamak Scrape-off Layer", Nucl. Fusion 24 (1984) 39.

18. M. F. A. Harrison, E. S. Hotston and A. de Matteis, "Plasma Edge Physics for NET/INTOR", NET Report no. 50 EUR-FU/XII-361/86/50, December 1985.

19. M. Petravic, D. Heifetz, S. Heifetz and D. Post, "Recent Progress in the Tokamak Edge Modeling", J. Nucl. Mater. 128 & 129 (1984) 91.

20. J. Neuhauser and R. Wunderlich, "A Radially Continuous Two Chamber Model for the High Recycling Divertor Edge Layer", to be published in J. Nucl. Mater. (1986).

21. M. Z. Hasan and R. W. Conn, "A Two-Dimensional Finite Element Multigroup Diffusion Theory for Neutral Atom Transport in Plasmas", UCLA Center for Plasma Physics and Fusion Engineering Report PPG-916 (February 1986) (to be published in J. Comp. Phys.)

22. K. Audenaerde, G. A. Emmert and M. Gordinier, "SPUDNUT: A Transport Code for Neutral Atoms in Plasmas", J. Comp. Phys. 34 (1980) 268.

23. J. A. Koski and J. B. Whitley, "Evaluation of Cooling Channel Configurations for Actively Cooled Limiters", Fus. Tech. 10 (1986) 789.

24. W. R. Gambill, R. D. Bundy and R. W. Winsbrough, "Heat Transfer, Burnout and Pressure Drop for Water in Swirl Flow through Tubes with Internal Twisted Tapes", Chem. Eng. Prog. Symp., Section 57 (1961) 127 (cited in W. H. Rohsenow, Handbook of Heat Transfer, McGraw-Hill, New York, 1973).

25. S. L. Milora, S. K. Combs and C. A. Foster, "A Numerical Model for Swirl Flow Cooling in High Heat Flux Particle Beam Targets and the Design of a Swirl Flow Based Plasma Limiter", Nucl. Engrg. & Des./Fusion 3 (1986) 301.

26. S.K. Combs, S. L. Milora, C. A. Foster et al., "Compact Inexpensive Target Design of Steady State Heat Removal in High Heat Flux Fusion Applications", Rev. Sci. Instrum. 56 (1985) 1526.

27. J. G. Collier, "Convective Boiling and Condensation", McGraw-Hill, London, 1972.

28. J. R. S. Thom et al., "Boiling in Subcooled Water during Flow up Heated Tubes or Annuli", Paper presented at the Symposium on Boiling Heat Transfer in Steam Generating Units and Heat Exchangers, Manchester, U. K., September 1965.

29. R.J. Price, Private communication, GA Technologies Inc., San Diego CA (1986).

30. M. DalleDonne et al., "Conceptual Design of Two Helium Cooled Fusion Blankets (Ceramic and Liquid Breeder) for INTOR", Kernforschungszentrum Karlsruhe Report KfK 3584, EUR 7987e (1983).

31. J.N. Goodier, "Thermal Stress and Deformation", J. Appl. Mech. 24 (1957) 467.

32. C.F. McDonald, "The HTGR Gas Turbine", in "Thermal and Flow Design of Helium-Cooled Reactors", American Nuclear Society, La Grange Park, Illinois (1984).

33. B. Badger et al., "HIBALL - A Conceptual Heavy Ion Beam Driven Fusion Reactor Study", University of Wisconsin Report UWFDM-450 (June 1981).

34. W. M. Wells, "ORNL TNS Program: Evaluation of the Bundle Divertor", Oak Ridge National Laboratory Report ORNL/TM-6727 (November 1979).

35. W. M. Wells, "A System for Handling Divertor Ion and Energy Flux Based on a Lithium Droplet Cloud", Nucl. Tech./Fusion 1 (1981) 120.

36. K. A. Werley, J. G. Gilligan and G. H. Miley, "A High Flux Energy and Particle Collection Scheme for Divertors", Proceedings of the 11th Symposium on Fusion Technology, Oxford, U. K. (September 1980) 1223.

37. K. A. Werley and J. G. Gilligan, "The Temperature Distribution of a Sphere in a Directed Uniform Heat Flux", University of Illinois Fusion Studies Laboratory Report FSL-12 (May 1980).